Recent Advances in Electrospray Cooling for High-Heat-Flux Thermal Management: Mechanisms, Enhancements, and Challenges

Lingyu Wang[1], Hui Yue[1], Yong Kong[1], Jos Derksen[2], Yubiao Sun*[1]

[1]School of Interdisciplinary Science, Beijing Institute of Technology, Beijing 100081, China

[2]School of Engineering, University of Aberdeen, Aberdeen AB24 3UE, UK

Abstract:

The escalating power density in microelectronics necessitates advanced thermal management to transcend performance and reliability bottlenecks. Electrospray cooling (ESC), utilizing electrohydrodynamic (EHD) atomization to generate fine, charged droplets, has emerged as a superior high-heat-flux solution due to its high surface-to-volume ratio and exceptional evaporation efficiency. This paper provides a comprehensive review of recent breakthroughs in ESC technology.

First, the EHD fundamentals of ESC are reviewed by linking Maxwell electric stress, interfacial force balance, Taylor-cone formation, jet breakup, and charged-droplet generation. Second, spray-mode transition is analyzed as the key bridge between electric-field-driven atomization and cooling performance, with emphasis on how cone-jet stability, multi-jet emission, and jet instabilities regulate droplet size, velocity, charge, spray distribution, liquid-film renewal, and surface rewetting. Third, heat-transfer enhancement and CHF-delay strategies are critically discussed, including working-fluid formulation, voltage–flow-rate coupling, nozzle and emitter design, and surface modification, all of which affect liquid replenishment, vapor removal, boiling regulation, and dry-out suppression. Subsequently, dimensionless correlations, numerical simulations, and physics-informed prediction approaches are evaluated to

[1] *Corresponding author: Yubiao Sun, ybsun@bit.edu.cn

clarify the current capabilities and limitations of ESC performance prediction.

Finally, key challenges and future directions are identified, including environmentally compatible dielectric fluids, stable high-throughput operation, scalable nozzle arrays, coupled liquid–vapor transport surfaces, regime-aware predictive models, and reliable system integration. This review establishes a mechanism-oriented pathway from EHD atomization to wall-side heat-transfer limits and provides guidance for scalable, reliable, and energy-efficient ESC systems for next-generation high-power electronics.

Keywords: Electrospray cooling; Thermal management; Heat transfer enhancement; Critical heat flux (CHF); Electrohydrodynamics(EHD) atomization; Spray-mode transition; Predictive modeling

1 Introduction

With the rapid advancement of information technology, the computational capability and integration density of high-performance computing chips [1,2], high-power-density communication equipment [3], as well as lithium-ion batteries and power electronic modules in electric vehicles [4–7] continue to increase. This trend has resulted in a dramatic escalation in power dissipation per unit area, surpassing even 1000 W/cm² [8]. Consequently, thermal management has emerged as a critical bottleneck constraining device performance, reliability, and further miniaturization. Excessive junction temperatures not only induce performance degradation and increased power consumption but also significantly shorten device lifespan, potentially leading to catastrophic failure [9]. Therefore, advanced cooling technologies are urgently needed to remove ultra-high heat fluxes while ensuring compactness, energy efficiency, operational stability, and compatibility with device integration.

Current mainstream cooling solutions often prove inadequate to meet the heat dissipation requirements of next-generation ultra-high heat fluxes. Air cooling is constrained by the inherent low specific heat capacity and thermal conductivity of air; consequently, its heat dissipation capability is typically restricted to approximately 1 W/cm² [10,11]. . Single-phase liquid cooling improves thermal performance but remains constrained by the convective heat transfer coefficient(HTC) at the fluid–solid interface, with manageable heat fluxes typically around 100 W/cm² [12]. Phase-change cooling primarily encompasses heat pipes [13], jet impingement cooling [14], microchannel cooling [15,16] , and spray cooling, can achieve heat dissipation capacities exceeding 500 W/cm² by utilizing latent heat [10,14,17]. However, these technologies still face practical limitations, such as orientation sensitivity in heat pipes [18–20], high pressure drop and clogging in microchannels [21,22], and high pumping power or continuous liquid supply requirements in jet impingement systems [14,23].

Among phase-change cooling technologies, spray cooling enhances heat transfer through droplet impingement, liquid-film evaporation, nucleate boiling, and secondary nucleation. However, conventional pressure-driven or gas-assisted spray systems often require mechanical pumps, relatively high flow rates, complex atomization structures, or auxiliary gas supplies, which increase system volume, energy consumption, and integration complexity.

Electrospray cooling (ESC) uses electrohydrodynamic (EHD) forces rather than purely mechanical or pneumatic forces to atomize the working liquid [24,25]. Under a sufficiently strong electric field, charge accumulation at the liquid meniscus and the competition among electric stress, surface tension, viscous force, inertial force, and gravity lead to Taylor cone formation and jet breakup. In stable regimes, especially the cone-jet mode, the liquid can be disintegrated into fine charged droplets with relatively uniform size and controllable trajectories [26]. These droplets enhance surface wetting, liquid-film renewal, evaporation area, and bubble departure, allowing ESC to maintain high heat transfer coefficients at relatively low flow rates [27].

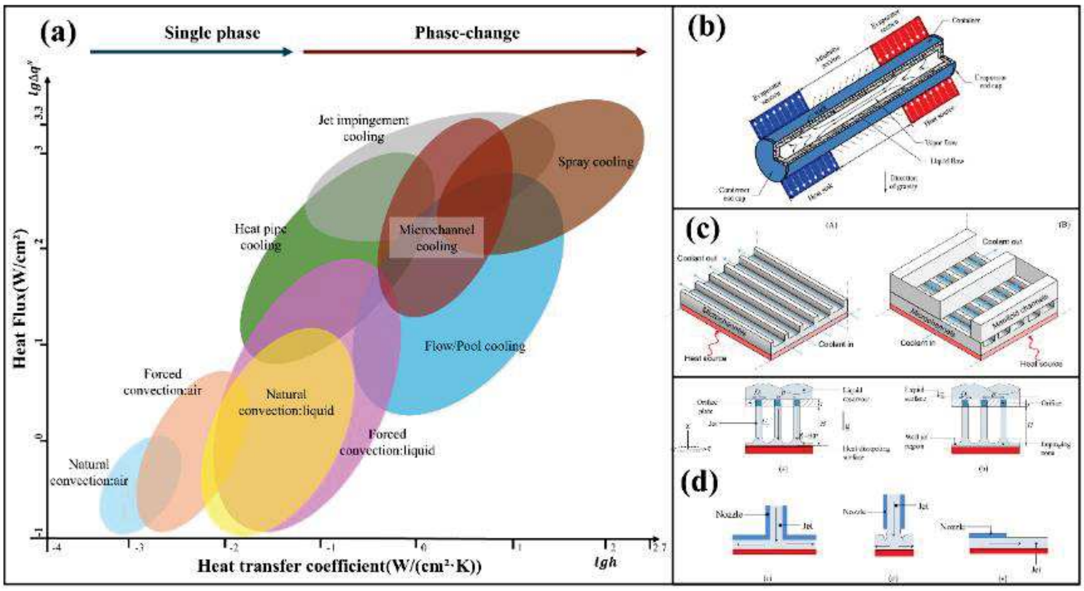

Fig. 1. Overview and mechanism of various advanced cooling technologies. (a) Comparative analysis of heat transfer performance under different cooling technologies. Reprinted from [28], Copyright [2022], by ASME; (b) Heat pipe cooling device [29]; (c) Microchannel cooling . Reprinted from Ref. [30] with permission from Elsevier (License No. 6194250072879); (d) Jet impingement cooling. Reprinted from Ref. [31] with permission from Elsevier (License No. 6194240710129).

Beyond thermal management, electrospray technology has been widely used in ionization mass spectrometry [32] (**Fig. 4(a)**), additive manufacturing [33] (**Fig. 4(b)**), combustion and propulsion [34] (**Fig. 4(c)**), microelectronics cooling [35] (**Fig. 4(d)**), inkjet printing [36] (**Fig. 4(e)**), pesticide spraying [37] (**Fig. 4(f)**), thin-film coating [38] (**Fig. 4(g)**), and drug delivery [39] (**Fig. 4(h)**). These applications demonstrate its ability to generate charged micro- or nano-droplets and to control mass transfer, material deposition, and droplet transport. For high-heat-flux cooling, however, ESC should be considered not only as an atomization technology, but also as a coupled electrohydrodynamic and phase-change heat transfer process.

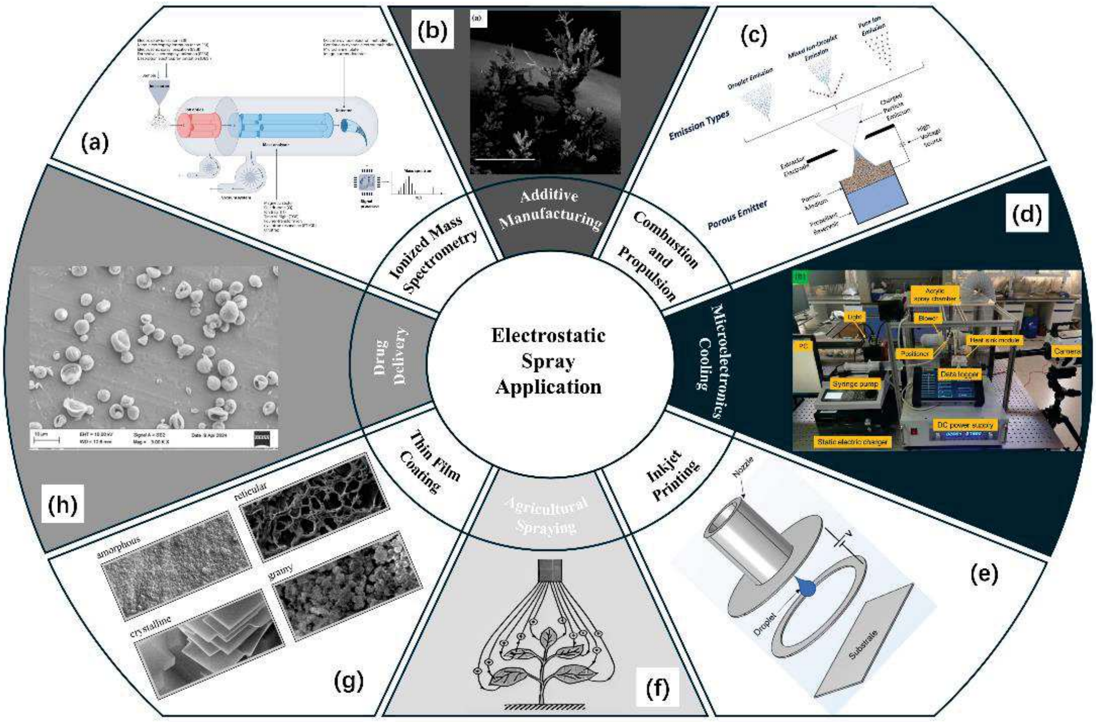

Fig. 2. Diverse applications of electrostatic spray technology in modern engineering and science. (a) Ionization mass spectrometry. Reprinted by permission from Springer Nature: Nature [32], copyright (2023); (b) Additive manufacturing [33]; (c) Combustion and propulsion [34]; (d) Microelectronics cooling. Reprinted from Ref. [35] with permission from Elsevier (License No. 6194280714176); (e) Inkjet printing. Reprinted by permission from Springer Nature: Nature [36], copyright (2025); (f) Pesticide spraying [37]; (g) Thin-film coating. Reprinted from Ref. [38] with permission from Elsevier (License No. 6194271043077) (h) Drug delivery. Reprinted by permission from Springer Nature: Nature [39], copyright (2025).

Although electrospray fundamentals and conventional spray cooling have been extensively reviewed [40–42], mechanism-oriented reviews focusing on ESC from the perspective of heat-transfer regulation remain relatively scarce. A recent review has provided a valuable overview of electrospray cooling and charged-droplet heat transfer [43], but further synthesis is still needed to explicitly connect EHD atomization, spray-mode evolution, wall-side liquid-film transport, boiling heat transfer, CHF delay, and predictive modeling. Existing electrospray studies mainly emphasize EHD atomization physics, Taylor-cone formation, spray-mode classification, scaling laws, and non-cooling applications [44–48], whereas the role of ESC as a low-power, coolant-saving, compact, and high-performance cooling strategy still requires further clarification from the perspective of coupled atomization and heat-transfer regulation. This review is therefore necessary because ESC provides a distinctive route for high-heat-flux thermal management through electrically driven fine-droplet atomization, charged-droplet transport, liquid-film renewal, and phase-change heat transfer.

The distinctive contribution of this review is to establish a mechanism-oriented framework for electrospray cooling by linking electric-field-induced atomization at the nozzle with spray-mode transition, droplet characteristics, wall interaction, and heat-transfer performance. In this framework, the EHD force balance, represented at the liquid–gas interface by Maxwell electric stress determine the onset and stability of spray modes, while the resulting droplet size, velocity, charge, and spatial distribution further affect liquid replenishment, surface rewetting, vapor removal, and CHF delay on the heated surface. On this basis, this review systematically discusses ESC enhancement strategies, including working-fluid regulation, voltage–flow-rate coupling, nozzle and emitter design, and surface modification. In addition, dimensionless correlations, numerical simulations, and physics-informed prediction approaches are reviewed to clarify the current status and limitations of ESC predictive modeling. This integrated perspective can help identify regime-dependent enhancement mechanisms and guide the development of scalable, reliable, and high-performance

ESC systems for high-heat-flux electronics cooling.

The remainder of this review is organized as follows. Section 2 establishes the thermal background by summarizing spray-cooling regimes and representative atomization-based cooling methods. Section 3 introduces the theoretical foundation and experimental characterization of ESC. Section 4 discusses spray-mode transition pathways and their heat-transfer implications. Section 5 reviews heat-transfer enhancement and CHF-delay strategies. Section 6 summarizes dimensionless correlations, numerical simulations, and physics-informed prediction methods. Finally, Section 7 presents the key conclusions and future research directions.

2 Spray Cooling Technology

Spray cooling technology facilitates heat exchange by atomizing liquid into fine droplets and impinging them upon a heated surface. It has been applied in data centers [49], power electronic modules, new energy vehicles, photovoltaic panels [42], aerospace [50], and lithium-ion batteries [51]. As shown in Fig. 2, with increasing surface superheat, spray cooling evolves from single-phase convection and liquid-film evaporation to nucleate boiling, transition boiling, and film boiling. The corresponding surface states, dominant mechanisms, and thermal consequences are summarized in Table 1.

A key limit in spray cooling is the critical heat flux (CHF), which refers to the maximum heat flux that can be sustained before heat-transfer deterioration occurs. Mechanistically, CHF is governed by the competition between liquid-film maintenance and vapor generation. At moderate surface superheat, droplet impingement, liquid-film spreading, and surface rewetting can continuously supply liquid to the heated wall, while bubble departure and vapor escape prevent excessive vapor accumulation. As the heat flux increases, however, vapor generation becomes stronger and may exceed the ability of the liquid film to replenish, rewet, and maintain effective liquid–solid contact. Under this condition, growing bubbles coalesce near the heated surface, local dry-out spots become stable, and the liquid film is progressively disrupted. Once dry-out regions become sufficiently extensive to interrupt continuous liquid–solid contact, CHF is reached, followed by increased thermal resistance and transition-boiling behavior [41].

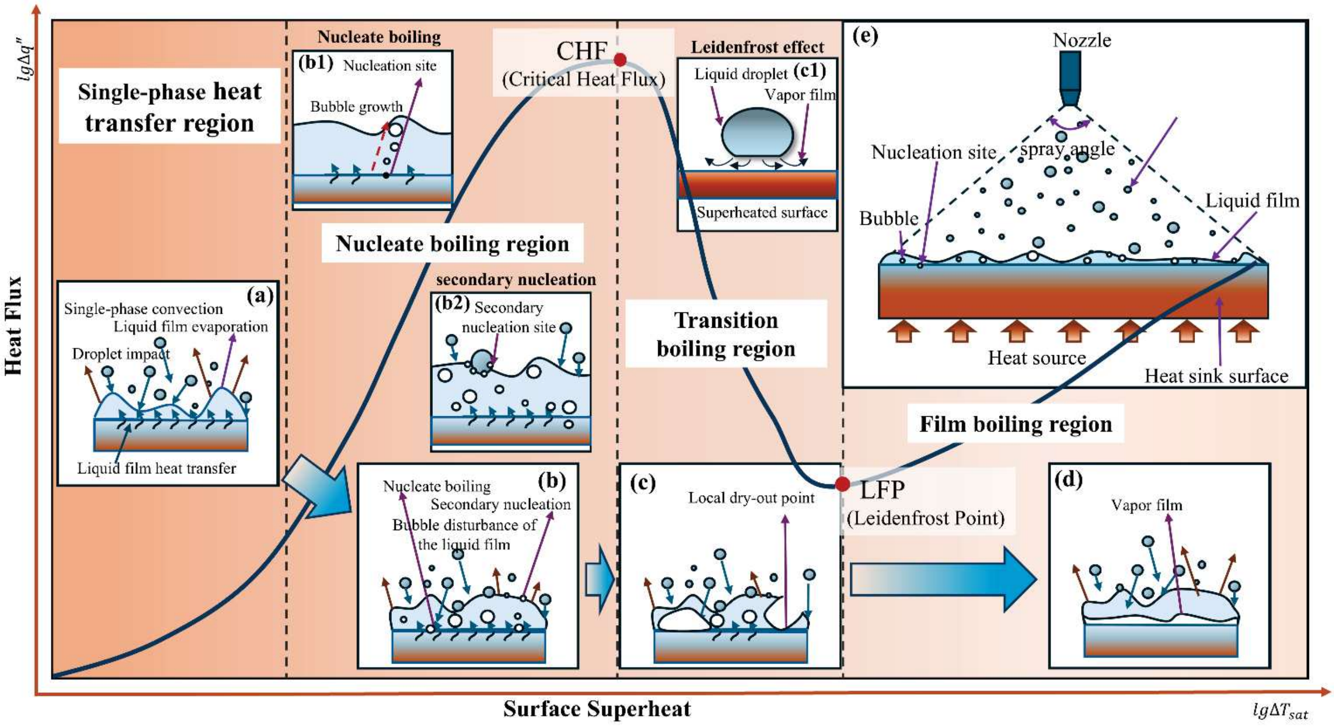

Fig. 3. Schematic illustration of the heat-transfer regimes and dominant mechanisms in spray cooling as a function of surface superheat. The main curve shows the transition from single-phase heat transfer to nucleate boiling, transition boiling, and film boiling. (a) Single-phase regime; (b) Nucleate boiling regime; (b1) Bubble nucleation and growth at surface nucleation sites. (b2) Secondary nucleation induced by droplet impact and liquid-film disturbance; (c) Transition boiling regime; (c1) Leidenfrost-effect; (d) Film boiling regime; (e) Overall spray cooling process. CHF denotes the critical heat flux, and LFP denotes the Leidenfrost point.

For ESC, CHF is further affected by the electrically controlled spray characteristics. The electric field regulates droplet size, charge density, spray morphology, impact distribution, and liquid-film dynamics [24,26,27,43,48,52]. Insufficient electric stress may produce large droplets, intermittent liquid delivery, or poor surface coverage, weakening liquid-film renewal and local rewetting. Excessive electric stress may induce jet oscillation, droplet splashing, non-uniform deposition, or off-target liquid loss, thereby reducing the effective liquid supply to the heated area. In addition, excessive liquid-film accumulation and poor surface wettability can increase conductive thermal resistance and weaken surface rewetting, while restricted vapor-escape pathways delay bubble departure, promote vapor accumulation, accelerate dry-spot expansion, and trigger premature CHF. Therefore, CHF in ESC is triggered by the loss of balance among electrically driven droplet supply, liquid-film renewal, surface rewetting, bubble departure, and vapor removal under high-heat-flux conditions. Reported ESC studies have demonstrated CHF values approaching approximately 100 W/cm^2 under optimized flow-rate, spray-mode, and nozzle-configuration conditions.

Based on atomization principles and driving mechanisms, common spray cooling methods include: pressure spray cooling (**Fig. 4(a)**), piezoelectric spray cooling (**Fig. 3(b)**), gas-assisted spray cooling (**Fig. 4(c)**), vacuum flash evaporation cooling (VFEC) (**Fig. 4(d)**), and electrospray cooling. Although these methods share the heat-transfer sequence shown in Fig. 3, their atomization mechanisms lead to different coolant consumption, droplet size, droplet transport, and spray distribution. These characteristics further affect liquid utilization, film uniformity, surface rewetting, and local dry-out tendency. Therefore, Table 2 summarizes the representative atomization characteristics and cooling implications of major spray cooling methods.

Table 1. Summary of heat-transfer regimes, dominant mechanisms, and thermal implications in spray cooling based on Fig. 3.

Heat-transfer regime	Related panel in Fig. 3	Dominant surface state	Main heat-transfer mechanisms	Heat-transfer trend and implication	Refs.
Single-phase / non-boiling regime	Fig. 3(a)	Droplets directly wet the surface and form a thin liquid film; no vapor bubbles are generated.	Droplet impingement, forced convection, sensible heating of droplets and liquid film, and non-boiling film evaporation.	Heat flux increases gradually with surface superheat. Heat transfer is mainly controlled by droplet velocity, surface coverage, and liquid-film renewal.	[53–56]
Nucleate boiling regime	Fig. 3(b), Fig. 3(b1)	Vapor bubbles nucleate at surface cavities within the liquid film.	Bubble nucleation, growth, departure, latent heat removal, and liquid-film disturbance.	Heat flux rises rapidly, and the heat-transfer coefficient is significantly enhanced. This is usually the most efficient heat-transfer regime.	[57,58]
Secondary nucleation	Fig. 3(b), Fig. 3(b2)	Droplets impinge on nucleation sites, bubbles, or disturbed liquid films.	Impact-induced nucleation, bubble detachment, local turbulence, and liquid-film renewal.	Interfacial heat transfer is further intensified. The process helps maintain high HTC before approaching CHF.	[54,57,59]
Critical heat flux	CHF point in Fig. 3	Local liquid supply becomes insufficient relative to evaporation and vapor generation.	Local dry-out initiation, reduced surface rewetting, and vapor accumulation.	CHF represents the upper heat-removal limit before heat-transfer deterioration. Delaying CHF is essential for safe high-heat-flux operation.	[41]
Transition boiling regime	Fig. 3(c)	Local dry spots appear, and liquid–solid contact becomes intermittent.	Coexistence of nucleate boiling and film boiling; unstable wetting and vapor blanketing.	Heat flux and HTC begin to decrease after CHF. Sustained operation in this regime should be avoided.	[41]
Film boiling regime	Fig. 3(d) Fig. 3(d1)	A continuous vapor film covers the heated surface;	Heat transfer occurs mainly through the vapor layer; droplets cannot effectively contact the wall.	Thermal resistance increases sharply, leading to severe heat-transfer degradation. The LFP marks the onset of stable film boiling.	[41,60]

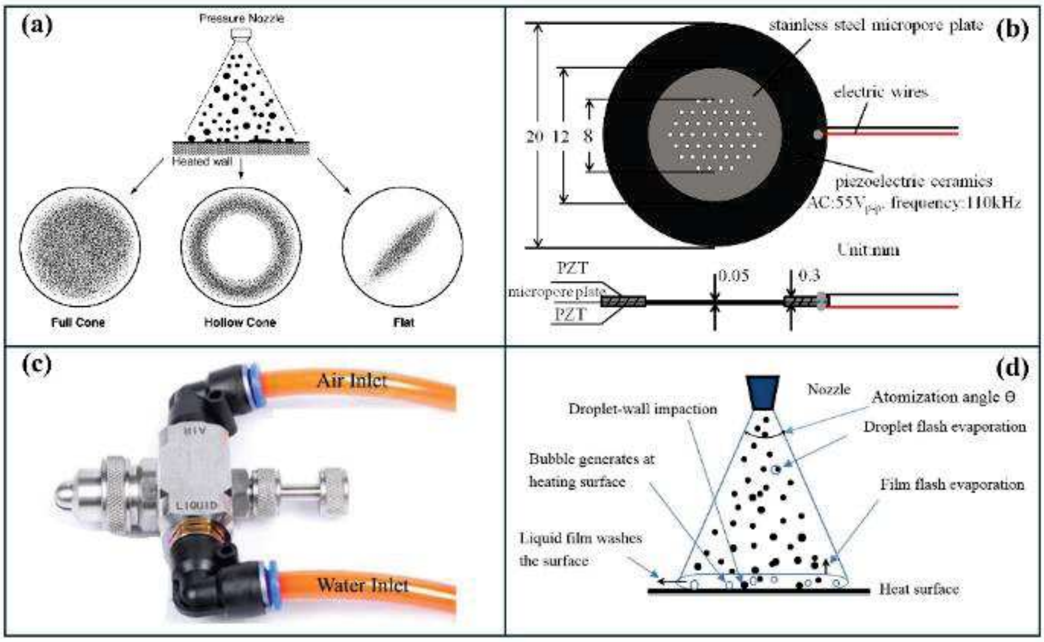

Fig. 4. Comparison of various atomization mechanisms and typical spray cooling configurations. (a) Pressure-atomized spray. Reprinted from Ref. [40] with permission from Elsevier (License No. 6194250482479); (b) Piezoelectric atomization spray. Reprinted from Ref. [61] with permission from Elsevier (License No. 6194250747301); (c) Air-assisted atomization. Reprinted from Ref. [62] with permission from Elsevier (License No. 6194250967273) (d) Vacuum flash evaporation atomization. Reprinted from Ref. [63] with permission from Elsevier (License No. 6194251174425).

As summarized in Table 2, ESC differs from mechanical or pneumatic sprays by using electric-field-driven atomization to generate fine, charged, and relatively uniform droplets at low flow rates. These droplets usually exhibit favorable transport characteristics and can promote surface wetting, thin-film spreading, and evaporation, which are beneficial for improving liquid utilization and delaying local dry-out. However, these cooling benefits strongly depend on spray-mode stability; excessive voltage, charge accumulation, corona discharge, or droplet over-dispersion may reduce the effective liquid flux reaching the heated surface and deteriorate cooling performance [24,25].

Table 2. Typical atomization characteristics and cooling implications of representative spray cooling methods

Item	Pressure spray cooling [40,64,65]	Piezoelectric spray cooling [61,66–68]	Gas-assisted / two-fluid spray cooling [69–71]	Electrospray cooling [24,26,27]
Coolant consumption / flow rate	Moderate to high; typically tens to hundreds of mL/min.	Low to moderate; reported values range from about 0.83 mL/min for a PZT atomizer to 2.4–37 mL/min for micro-nozzle PZT spray plates.	Moderate to high; liquid supply is coupled with gas consumption. Moderate to high; typically tens to hundreds of mL/min.	Low flow rate, typically several μL/min to several hundred μL/min per emitter; multiplexed systems may reach tens to about 100 mL/h.
Droplet size	Typically 50–300 μm.	Typically 50–150 μm; governed by frequency, orifice size, voltage, and liquid properties.	Typically 10–100 μm; optimized gas–liquid momentum exchange can reduce SMD below 40 μm.	Typically 1–50 μm; Deng and Gomez reported d10 ≈ 25 μm.
Droplet transport / distribution	High momentum; velocity typically 5–30 m/s. Spatial uniformity is moderate and sensitive to pressure and nozzle geometry.	Localized and controllable spray; Typical microspray velocities are several m/s, and the peak flow rate can reach 22.5 m/s. Relatively uniform droplets.	Adjustable but geometry-sensitive; velocity commonly 1–30 m/s, and distribution depends on Re, We, orifice size, and gas–liquid momentum ratio.	Several m/s, commonly around 7–9 m/s in representative ESC studies D. Highly uniform droplets in cone-jet and multi-jet modes.
Cooling implication	Strong liquid supply benefits high-heat-flux cooling, but pressure drop, clogging, and non-uniform coverage remain limitations.	Suitable for compact and localized low-flow cooling, but large-area scalability is limited by flow capacity and array integration.	Fine atomization and gas-driven disturbance can enhance cooling, but the gas supply increases system complexity and parasitic power.	Fine, charged, and uniform droplets at low hydraulic pressure promote spreading and thin-film evaporation; scale-up and mode stability remain key constraints.

Note: The values listed in this table represent typical ranges reported in representative spray-cooling and atomization studies rather than strict universal limits. Vacuum flash evaporation cooling is not included because its performance is governed primarily by chamber pressure, flash evaporation rate, droplet residence time, and liquid-film phase change rather than by nozzle-generated droplet size, velocity, and spatial dispersion. SMD or D32 denotes the Sauter mean diameter.

3 Electrospray principles and heat-transfer performance characterization

3.1 Fundamentals of Electrohydrodynamics (EHD)

Electrospray cooling is an electric-field-driven EHD atomization and heat-transfer process. This technique is realized by applying a high voltage between a nozzle and a grounded electrode. At the nozzle exit, charge accumulation and Maxwell electric stress act on the liquid–gas interface and compete with capillary pressure, viscous resistance, liquid inertia, gravity, and liquid-supply constraints. [72]. The balance among these forces determines liquid deformation, jet formation, and the subsequent spray modes, which are discussed in Section 4.Electrohydrodynamics describes the action of electric fields on non-uniform electrolyte fluids, the electric body-force density in EHD can be decomposed into three main contributions: [72]:

$$F_e = q_e E - 0.5E^2 \nabla \varepsilon_l + 0.5\nabla\left[E^2\left(\frac{\partial \varepsilon_l}{\partial \rho}\right)\rho_l\right] \quad (1)$$

where q_e represents the liquid charge density, E represents the electric field strength, ε_l represents the liquid permittivity, and ρ represents the liquid density.

The three terms on the right-hand side of Eq. (1) represent the free-charge Coulomb force, the polarization or dielectrophoretic force, and the electrostrictive force, respectively [46,72,73]. The Coulomb force arises from the interaction between the electric field and free charges in the liquid. In electrospray, these charges are transported toward the liquid－gas interface and accumulate near the meniscus apex, where electrical momentum is transferred to the liquid and promotes axial motion toward the nozzle exit [45,46,74]. The polarization force originates from spatial gradients in permittivity and becomes important near the liquid－gas interface, where dielectric discontinuity modifies the electric traction acting on the curved meniscus [45,46,72,73]. The electrostrictive force is associated with the dependence of permittivity on liquid density and mainly appears as a pressure-like volumetric stress; for weakly compressible or incompressible liquids, it is often absorbed into the pressure field [46,72,73]. Therefore, (1) identifies the sources of electric forcing in the liquid, while the Maxwell-stress description explains how this forcing is transmitted to the liquid – gas interface and converted into meniscus deformation [45,46,74–76].

At the nozzle exit, the Maxwell electric stress can be resolved into normal and tangential components. The normal component deforms the meniscus against capillary pressure, whereas the tangential component drives interfacial shear, surface-charge convection, and axial liquid motion toward the meniscus apex [74–76]. As Maxwell electric stress increases relative to capillary pressure, viscous resistance, liquid inertia, gravity, and liquid-supply constraints, the emission behavior evolves from dripping or micro-dripping to spindle-like breakup and, within a finite stability window, to cone-jet mode [45,77–79]. In the cone-jet regime, a quasi-steady balance between normal electric stress and capillary pressure forms a Taylor cone, whose theoretical semi-vertical angle is approximately 49.3° under static equilibrium [45,46,74–76]. If the applied voltage or flow rate exceeds the stable operating window, this balance may be disrupted, leading to intermittent cone-jet, multi-jet, whipping, or simple-jet regimes [80–82]. Therefore, spray-mode transition should be understood as a coupled force-balance process rather than as a result of voltage or flow rate variation alone.

Among the various electrospray modes, the cone-jet mode is one of the most stable atomization regimes and is therefore widely used in electrospray cooling studies. A quantitative description of the Taylor cone is essential for linking the interfacial force balance to jet formation and droplet generation.

de la Mora summarized theoretical descriptions of the static Taylor cone [76], in which the liquid surface morphology is governed by the balance between electrostatic and capillary pressures [75]:

$$\sigma\nabla\cdot n-\frac{1}{2}\varepsilon_0(\nabla\phi)^2=\Delta p \tag{2}$$

Where ϕ represents electric potential, and Δp represents the pressure difference across the interface. When the applied electric field strength is sufficient to overcome surface tension, the liquid surface stabilizes into a Taylor cone with a semi-vertical angle of approximately 49.3°. The critical voltage follows the scaling relationship [75]:

$$V \sim \left(\frac{\sigma d}{\varepsilon_0} \right)^{1/2} \tag{3}$$

where d represents the characteristic dimension of the nozzle or capillary. Furthermore, in the steady cone-jet mode, the spray current and jet diameter satisfy the following scaling laws [75,83]:

$$I \sim (KQ)^{1/2} \tag{4}$$

$$d_j \sim \left(\frac{Q\varepsilon_0}{K} \right)^{1/3} \tag{5}$$

where K is the liquid electrical conductivity, Q is the flow rate, and d_j is the jet diameter.

These scaling relationships provide the quantitative link between the Taylor-cone force balance and the droplet-scale characteristics produced downstream. The spray current reflects charge transport from the meniscus into the emitted jet, while the jet diameter determines the characteristic length scale before primary breakup. Therefore, Q controls liquid supply to the cone-jet, whereas K affects charge relaxation and current transport. Their combined influence on I and d_j further affects droplet number flux, charge-to-mass ratio, spray stability, and liquid replenishment capacity during electrospray cooling [45,46,76,79].

After the charged jet is emitted from the Taylor cone, it undergoes primary breakup mainly through capillary instability. Since the resulting droplets carry electric charge, electrostatic repulsion and Rayleigh-limit effects further influence droplet dispersion and possible secondary breakup [45,84].

The number of free charges carried by a droplet affects its size. Rayleigh's theory indicates that free charges in a dielectric liquid reduce the effective surface tension. When the charge density exceeds a critical limit, surface tension is no longer sufficient to maintain the liquid shape, leading to interfacial instability. This limiting condition is known as the Rayleigh limit and is expressed as [84]:

$$\sigma_e = \sigma - \frac{q_e^2}{8\pi^2 \varepsilon_0 d^3} \tag{6}$$

where σ_e and σ denote the surface tension coefficients of the charged liquid and the neutral liquid, respectively; ε_0 represents the permittivity of the environment; and d represents the droplet diameter.

In summary, the combined action of EHD forces and other competing forces constitutes the upstream physical basis of electrospray atomization. They link operating parameters and liquid properties, including applied voltage, flow rate, electrical conductivity, permittivity, viscosity, surface tension, and nozzle geometry, to droplet-scale variables such as jet diameter, droplet size, charge level, velocity, emission frequency, spray angle, and spatial distribution. These variables serve as the boundary conditions for the spray-mode classification, droplet-surface interaction, liquid-film renewal, and interfacial heat-transfer analysis discussed in the following sections.

3.2 Experimental Realizations of Electrospray Cooling

Generally, an electrospray cooling experimental system comprises three subsystems: the electrospray system, the heating system, and the image and data acquisition system. The experimental setup and its connections are illustrated in **Fig. 5(a)** and **Fig. 5(b)**, respectively. The electrospray system typically includes a high-voltage DC power supply, a syringe pump, and a capillary nozzle. The heating system provides a controllable heat load through a heating block or simulated heat source, while the image/data acquisition system records spray morphology, liquid-film behavior, temperature signals, and electrical parameters.

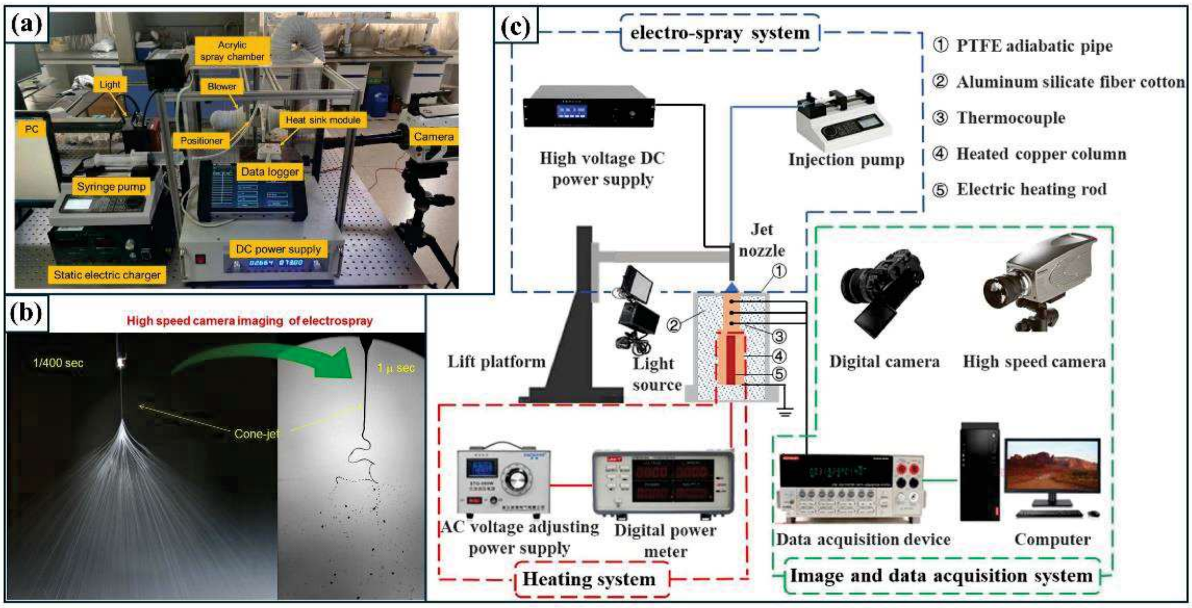

Fig. 5. Experimental configuration and mechanism of the electrospray cooling system. (a) Experimental apparatus for electrostatic spray cooling. Reprinted from Ref. [35] with permission from Elsevier (License No. 6194280714176);(b) Electrostatic spray cooling nozzle structure. Reprinted from Ref. [78] with permission from Elsevier (License No. 6194280109434);(c) Schematic illustration of the electrostatic spray cooling process. Reprinted from Ref. [85] with permission from Elsevier (License No. 6194281377302).

Furthermore, since the observed electrospray morphology is sensitive to the exposure time of the high-speed camera, the same cone-jet mode may appear either as a seemingly stable conical spray or as an oscillating jet undergoing droplet breakup [78], as shown in **Fig. 5(c)**.

In typical electrospray cooling experiments, data processing follows standard heat-transfer data reduction procedures to ensure physical consistency and comparability. As summarized in **Fig. 6,** the workflow mainly includes heat balance calculation, surface temperature determination, heat-transfer coefficient and CHF evaluation, and dimensionless analysis. First, the temperature gradient inside the heating block is measured using embedded thermocouples. Assuming one-dimensional steady-state thermal conduction, the surface heat flux can be calculated using Fourier's law:

$$q = k_{Cu} \frac{\Delta T}{\Delta x} \tag{7}$$

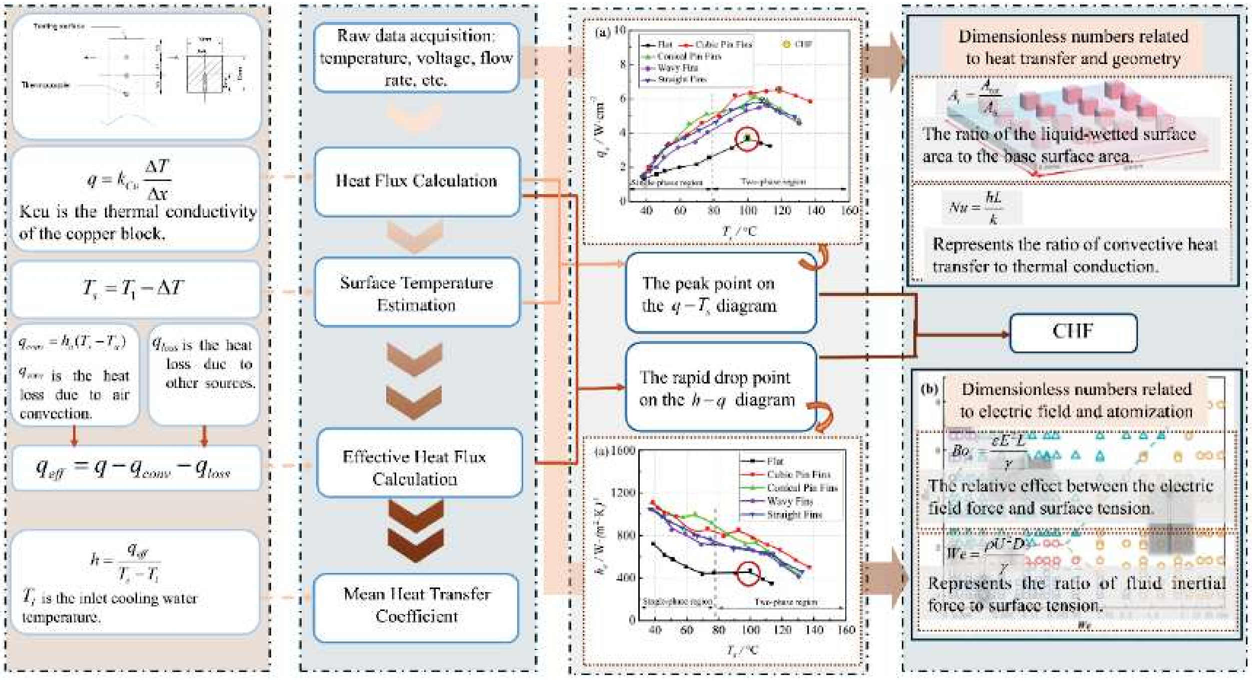

Fig. 6. Data processing and analysis workflow for electrospray cooling experiments.

where k_{Cu} is the thermal conductivity of the heating block material (copper), ΔT is the temperature difference between measurement points, and Δx is the distance between the two points. The surface temperature of the heated surface is further extrapolated as:

$$T_s = T_1 - \Delta T \tag{8}$$

T_1 is the temperature of the first thermocouple near the surface. To obtain the effective heat flux, environmental heat loss is corrected using natural-convection estimation, numerical simulation, or experimental calibration:

$$q_{eff} = q - q_{conv} - q_{loss} \tag{9}$$

$$q_{conv} = h_a(T_s - T_a) \tag{10}$$

Where h_a is the air convective heat transfer coefficient, and T_a is the ambient temperature. Subsequently, the average heat transfer coefficient can be derived based on the effective heat flux and the liquid temperature difference:

$$h = \frac{q_{eff}}{T_s - T_l} \tag{11}$$

By plotting the $q - T_s$ and $h - q$ curves, heat transfer characteristics can be analyzed and the CHF determined. Specifically, CHF is determined by the peak of the curve, while the point of rapid decline reflects the transition and deterioration of heat transfer performance.

In electrospray cooling research, various dimensionless numbers are typically introduced to characterize experimental conditions and heat transfer intensity. The electric Bond number (Bo_E) quantifies the ratio between electrical stresses and surface tension forces. The Weber number (We), defined as the ratio of inertia to surface tension, serves as a metric for evaluating droplet disintegration. The Nusselt number (Nu) is defined as the ratio of convective heat transfer to thermal conduction, serving to compare the degree of convective enhancement under different spray states:

$$We = \frac{16 \rho_l D_o Q^2}{\pi^2 D_i^4 \sigma} \tag{12}$$

$$Bo_E = \frac{\varepsilon_0 D_o E_0^2}{2\sigma} \tag{13}$$

$$Nu = \frac{hL}{k} \tag{14}$$

Here, D_o and D_i denote the capillary's outer and inner diameters, respectively, while Q signifies the fluid's volumetric flow rate.

For surfaces with macroscopic structures, the area ratio is defined to quantitatively evaluate the heat transfer enhancement effect resulting from the synergy between surface modification and the electric field.

$$A_r = \frac{A_{tot}}{A_b} \tag{15}$$

$$A_{tot} = A_b + A_s \tag{16}$$

4 Mode-transition pathways and heat-transfer implications of electrospray cooling

Building on the EHD force-balance framework discussed in Section 3.1, this section focuses on how different electrospray modes translate into distinct droplet-scale and surface-scale cooling conditions.

Geometric classification is the most intuitive and prevalent approach for investigating electrospray modes, mainly based on the liquid-meniscus morphology at the nozzle exit and the macroscopic spray pattern [26,45,46,77,86]. Different modes generate different downstream boundary conditions at the heated surface, including droplet size distribution, impact velocity, arrival frequency, spatial flux distribution, and liquid-film replenishment behavior [48,85,87,88]. These boundary conditions not only determine the heat-transfer coefficient under normal operating conditions but also influence the tendency toward local dry-out and the available CHF margin under high heat flux.

Mode transition is governed by the coupled effects of operating parameters, including the applied voltage, flow rate, and fluid properties such as electrical conductivity, viscosity, and surface tension. To quantify the relative importance of liquid inertia, Maxwell electric stress, and capillary effects, two key dimensionless numbers, We (**Eq. (12)**) and Bo_E (**Eq. (13)**), are introduced.

In electrospray cooling, relatively low flow rates are commonly employed to maintain a stable cone-jet mode, which generally corresponds to low We. Therefore, the spray-mode evolution can be discussed along two representative pathways under low-We and high-We conditions. As shown in Fig. 7, these pathways illustrate how electrospray modes evolve with increasing Bo_E, from dripping-like emission to cone-jet and multi-jet regimes at low We, and from simple-jet behavior to varicose and whipping instabilities at high We.

At low We and low Bo_E numbers, the spray exhibits a dripping mode (**Fig.**

7(e)), where surface tension and gravity dominate and droplet diameter larger than the nozzle detach periodically [78,89,90]. This localized and low-frequency liquid supply is unfavorable for uniform surface replenishment. As the Bo_E number increases, electric stress becomes comparable to capillary stress, causing stronger meniscus elongation, smaller emitted droplets, and transition to micro-dripping mode (**Fig. 7(d)**) [91,92]. With a further increase in Bo_E, Maxwell electric stress periodically exceeds the capillary restoring stress but cannot yet maintain a steady cone-jet balance. The meniscus is then stretched into spindle-shaped ligaments before pinch-off, forming spindle mode (Fig. 7(c)) [78,79]. These periodic regimes involve intermittent droplet supply and limited spray coverage, and are therefore less favorable for uniform liquid-film renewal than continuous spray modes.

As the Bo_E number increases, when the normal electric stress quasi-steadily balances capillary pressure and tangential electric stress continuously drives interfacial shear and liquid supply toward the meniscus apex, the cone-jet mode is established (**Fig. 7(b)**). In this regime, a steady Taylor cone emits a thin continuous jet, which breaks into small and relatively uniform droplets [26,48,52]. For cooling applications, the small droplet size, high emission frequency, and stable spray dispersion promote surface coverage, thin-film renewal, and local rewetting, thereby helping suppress dry-out and improve CHF [48]. However, cone-jet stability exists only within a finite operating window. When electric forcing, flow rate, or jet charge level becomes excessive, the emitted jet may undergo varicose or whipping instability, leading to broader spray dispersion and a wider droplet spatial distribution [80,93].

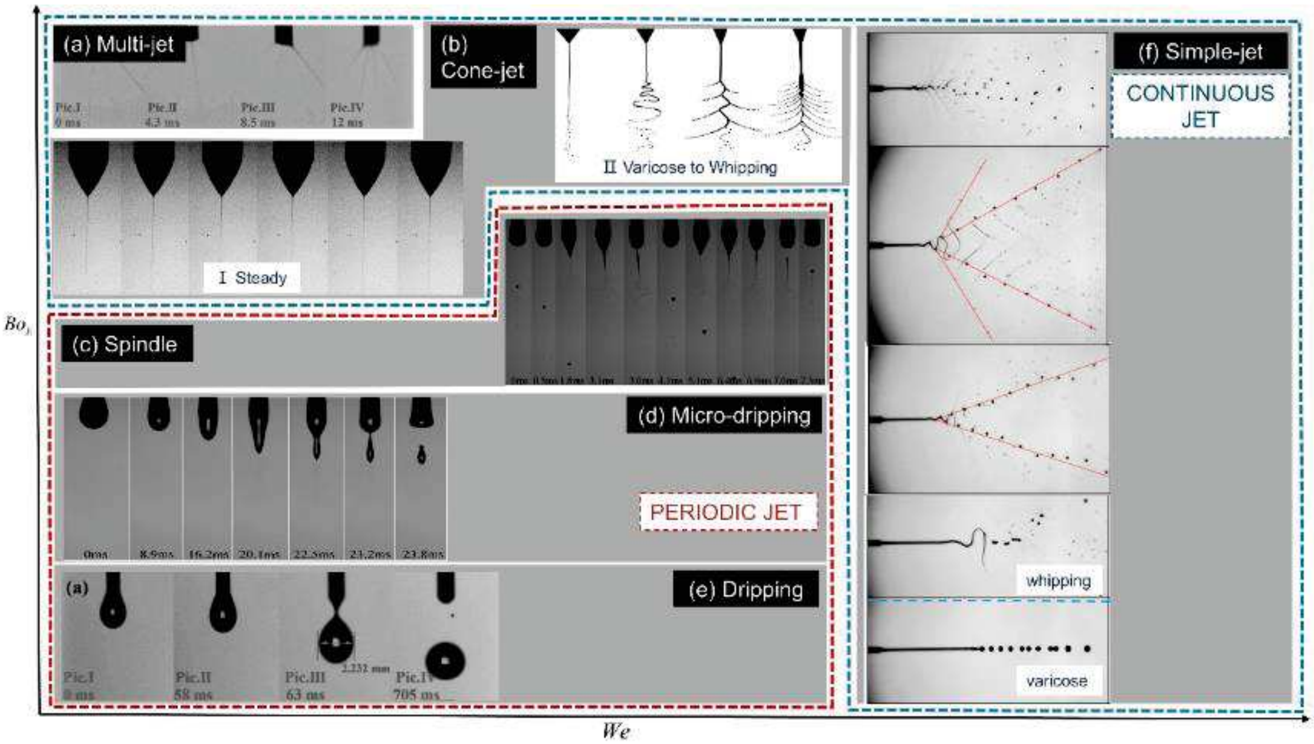

Fig. 7. Classification and Variation of Electrostatic Spray Modes under Different Bo_E and We. Periodic jet modes include (c) spindle, (d) micro-dripping, and (e) dripping, whereas continuous jet modes include (a) multi-jet, (b) cone-jet, and (f) simple-jet modes. The working fluid is anhydrous ethanol in all cases. (a) **Multi-jet mode** at (Q = 15) mL/h and (V = 5) kV. Reprinted from Ref. [87] with permission;(b) **Cone-jet mode and varicose-to-whipping transition** (Q = 80 nL/s, V = 3.70 kV). Reprinted from Ref. [94] with permission from Elsevier (License No. 6194300208596);(c) **Spindle mode** (Q = 0.05 mL/min, V = 5.8 kV). Reprinted with permission from Ref. [44]. Copyright 2024 AIP Publishing;(d) **Micro-dripping mode** (Q = 0.05 mL/min, V = 3.3 kV). Reprinted from Ref. [79]with permission from Elsevier (License No. 6194300883105);(e) **dripping mode** (Q = 15 mL/h, V = 0 kV). Reprinted from Ref. [87] with permission;(f) **Simple jet mode**: transition from axisymmetric to whipping instability at Q = 100 mL/h (We = 9.58), with V increasing from 0 kV (Bo_E = 0) to 10.96 kV (Bo_E = 4.10). Reprinted with permission from Ref. [95] Copyright 2022 AIP Publishing.

With further increase in Bo_E, charge accumulation and electric stress become sufficiently strong to destabilize the single emission site, resulting in multi-jet mode (**Fig. 7(a)**), where multiple jets coexist near the nozzle rim [87]. This mode can enlarge the spray footprint and increase the number of impacting droplets [45,77,87]. Wan et al. reported that cone-jet and multi-jet modes produced smaller droplets, higher velocities, and larger spray cone angles than periodic regimes, thereby improving heat flux under their tested conditions [87]. However, excessive dispersion may reduce the effective incident flux on the target surface and deteriorate cooling performance [87,96].

The simple-jet mode (**Fig. 7(g)**) typically forms at larger We, where the liquid jet manifests as a continuous column dominated by strong liquid inertia rather than originating from a stable Taylor cone [81]. With increasing voltage or flow rate, the jet may evolve from axisymmetric varicose instability to non-axisymmetric whipping instability. Varicose instability produces surface waves and relatively large droplets with a broad size distribution [97], whereas whipping instability causes jet bending, larger spray angles, and more dispersed droplet deposition [81,85]. For cooling, the simple-jet mode can provide higher liquid throughput and stronger impact momentum, which may enhance surface replenishment under large heat loads. However, excessive liquid supply or jet oscillation can lead to thick liquid films, flooding, splashing, or off-target liquid loss [27,81,96]. Shao et al. showed that stable jetting enhanced heat flux and CHF, whereas excessive oscillation reduced CHF and the maximum heat-transfer coefficient by splashing coolant away from the heated surface [27].

Although the transition sequence among dripping, micro-dripping, spindle, cone-jet, simple-jet, and multi-jet modes can be qualitatively summarized, their quantitative thresholds are strongly apparatus- and fluid-dependent. For ESC applications, the stable cone-jet mode is particularly important because it provides fine, relatively uniform charged droplets and stable liquid replenishment. Therefore, in Section 5.2, we further discuss the operating window of the cone-jet mode and examine its dependence on

Bo_E, We, applied voltage, flow rate, and nozzle geometry.

In ESC, the cooling effect of each mode is determined by the droplet- and liquid-film-scale boundary conditions it generates, including droplet size, impact velocity, emission frequency, charge level, spray angle, spatial flux distribution, liquid-film thickness, surface rewetting, and vapor removal. Continuous and well-controlled modes, especially stable cone-jet, multi-jet, and stable simple-jet regimes, generally favor liquid-film renewal and dry-out suppression, whereas periodic modes or excessive whipping may cause intermittent supply, non-uniform deposition, thick-film accumulation, or off-target liquid loss. Thus, spray-mode classification links operating parameters and fluid properties to surface boundary conditions, ultimately affecting HTC and CHF.

5 Heat transfer enhancement and CHF-delay strategies in electrospray cooling

Heat-transfer enhancement in ESC should be evaluated not only by the instantaneous heat-transfer coefficient but also by the ability to sustain effective liquid–solid contact and delay CHF under high heat flux. In this context, enhancement strategies should first improve droplet delivery, liquid-film renewal, surface rewetting, vapor removal, and the critical heat flux (CHF) margin. By strengthening liquid replenishment and vapor discharge while suppressing localized dry-out, these mechanisms help extend the stable nucleate-boiling regime and prevent premature transition to film boiling. Research targeting cooling enhancement mechanisms primarily focuses on three aspects: cooling working fluids, spray parameters, and surface modification.

5.1 Enhancement Effects of Working Fluids on Electrospray Cooling

The thermophysical properties of the coolant, such as surface tension, boiling point, specific heat capacity, thermal conductivity, and latent heat of vaporization, profoundly influence the morphology and mode of the electrospray, as well as liquid-film evaporation, bubble nucleation, and surface rewetting, thereby determining both the heat-transfer coefficient and the CHF under high heat flux.

Water and ethanol have been widely used in ESC studies because their relatively high electrical conductivity facilitates charge relaxation and stable cone-jet formation [27,48,82,92,96]. However, their corrosivity, limited dielectric strength, and relatively high boiling points restrict their direct use in microelectronic cooling, where excessive wall superheat may damage electronic components before efficient nucleate boiling is activated.

Dielectric liquids and dielectric-based mixtures have therefore been introduced to balance EHD atomization stability with electrical insulation. In the modification of dielectric fluids, Tian et al. [35] investigated an ethanol–R141b mixture and found that an ethanol mass concentration of 20–50% effectively leverages the high thermal conductivity and latent heat of ethanol, achieving a maximum HTC of 1.9 kW/($m^2 \cdot K$). However, excessive ethanol concentrations lead to a surge in surface tension and viscosity, which hinders atomization and induces liquid film flooding, thereby deteriorating heat transfer. The effects of ethanol mass concentration on spray morphology, HTC, Sauter Mean Diameter (SMD), droplet average velocity, and spray angle are shown in **Figs. 8(a)** and **(b)**. Given the high ozone-depletion potential of R141b, future dielectric-fluid design should shift toward environmentally benign, low-GWP alternatives such as hydrofluoroolefins (HFOs) [98]. Similarly, Xu et al. [85] studied the heat transfer characteristics of an HFE-7100–ethanol mixture. The results indicated that a moderate addition of ethanol (4%–8%) improves heat transfer in the low-temperature single-phase region by enhancing thermal conductivity. Although a higher concentration (15%) enhances performance in the two-phase region via high latent heat, it suppresses convection in the single-phase region due to reduced volatility. Consequently, an ethanol concentration of 8% serves as an optimal trade-off, effectively balancing droplet charging capacity with evaporation rates, and reconciling heat transfer performance across both single-phase and two-phase regions. The effects of ethanol concentration in HFE-7100 mixtures on electrospray morphology and surface heat flux are shown in **Figs. 8(c)** and **(d)**. The physical properties of water, ethanol, dielectric liquids, and their mixtures are summarized in Table 3.

In addition to deionized water, ethanol, dielectric liquids, and their mixtures, common cooling media for spray cooling also include ethylene glycol [87], isopropanol [99], and methanol [100]. Furthermore, adding soluble salts, soluble alcohols, surfactants, and nanoparticles to single-component coolants represents a common modification strategy.

The introduction of nanofluids aims to transcend the thermal property limits of conventional cooling media. Early theoretical studies primarily focused on the enhancement of thermal conductivity, postulating that nanoparticle aggregation [101,102] and the liquid-solid interfacial nanolayer [103,104] are the dominant mechanisms for thermal enhancement, whereas the contribution of Brownian motion is relatively minor [105,106]. However, beyond improving bulk thermal conductivity, the way nanoparticles deposit onto the hot surface is even more critical. The rough porous layer formed by deposition not only increases boiling nucleation sites but also significantly improves the spreadability and rewetting capability of the working fluid by modifying surface tension and contact angles [107].

Table 3: Physical Properties of Common Liquid Media in Electrostatic Spray

Property	**Density**	**Surface tension coefficient**	**Boiling point**	**Electrical conductivity**	**Thermal conductivity**	**Specific heat**	**Latent heat**
Unit	kg/m³	N/m	◦C	S/m	W/m·K	J/kg·K	kJ/kg
Water	997	0.072	100	~10^{-6}-10^{-4}	0.598	4182	2257
Ethanol	789	0.0219	78	~5×10^{-5}	0.171	2480	837.36
HFE-7100	1500	0.0142	61	~7×10^{-10}	0.068	1183	111.6
8vol%Ethanol/ 92vol%HFE7100	1436	0.0142	-	4×10^{-5}	≈0.069	2408	805.4
R141b	1227	0.018	32.1	~10^{-10}	~0.079	≈1160	~223
50%volR141b/ 50%volEthanol	1000	0.0204	-	~10^{-5}	≈0.125	≈1820	~5×10^{2}

Mixture Property Calculation Formulas	[108]	$P_i = \frac{\sigma_i^{1/4} M_i}{\rho_{L,i} - \rho_{V,i}}$ $P_{\text{mix}} = \sum_i x_i P_i$ $\sigma_{\text{mix}} = \left[\frac{P_{\text{mix}} \left(\rho_{L,\text{mix}} - \rho_{V,\text{mix}} \right)}{M_{\text{mix}}} \right]^4$ [109,110]	-	$K_{\text{mix}} = \sum_i \phi_i K_i$ [111]	$k_{\text{mix}} = \sum_i \phi_i k_i$ [112]	$c_{p,\text{mix}} = \sum_i w_i c_{p,i}$ [113]	$h_{fg,\text{mix}} = \sum_i w_i h_{fg,i}$ [113]
Parameter Definitions	ρ_i : Density of component i, ϕ_i : Volume fraction of component i in the mixture.	-	-	K_i : Electrical conductivity of component i, ϕ_i : Volume fraction of component i in the mixture.	k_i : Thermal conductivity of component i, ϕ_i : Volume fraction of component i in the mixture.	$c_{p,i}$: Specific heat (at constant pressure) of component i, w_i : Mass fraction of component i.	$h_{fg,i}$: Latent heat of vaporization of component i, w_i : Mass fraction of component i.
Notes	Assume that the overall volume change is negligible during mixing.	Assume that the liquids are completely miscible and do not undergo chemical reactions.	The polarity difference is significant, making it difficult to calculate.	For order-of-magnitude calculations only, experimental measurements are recommended.	Assume that the liquids are completely miscible and do not undergo chemical reactions.	Assume no phase or chemical reaction occurs during mixing.	Suitable for engineering estimates.

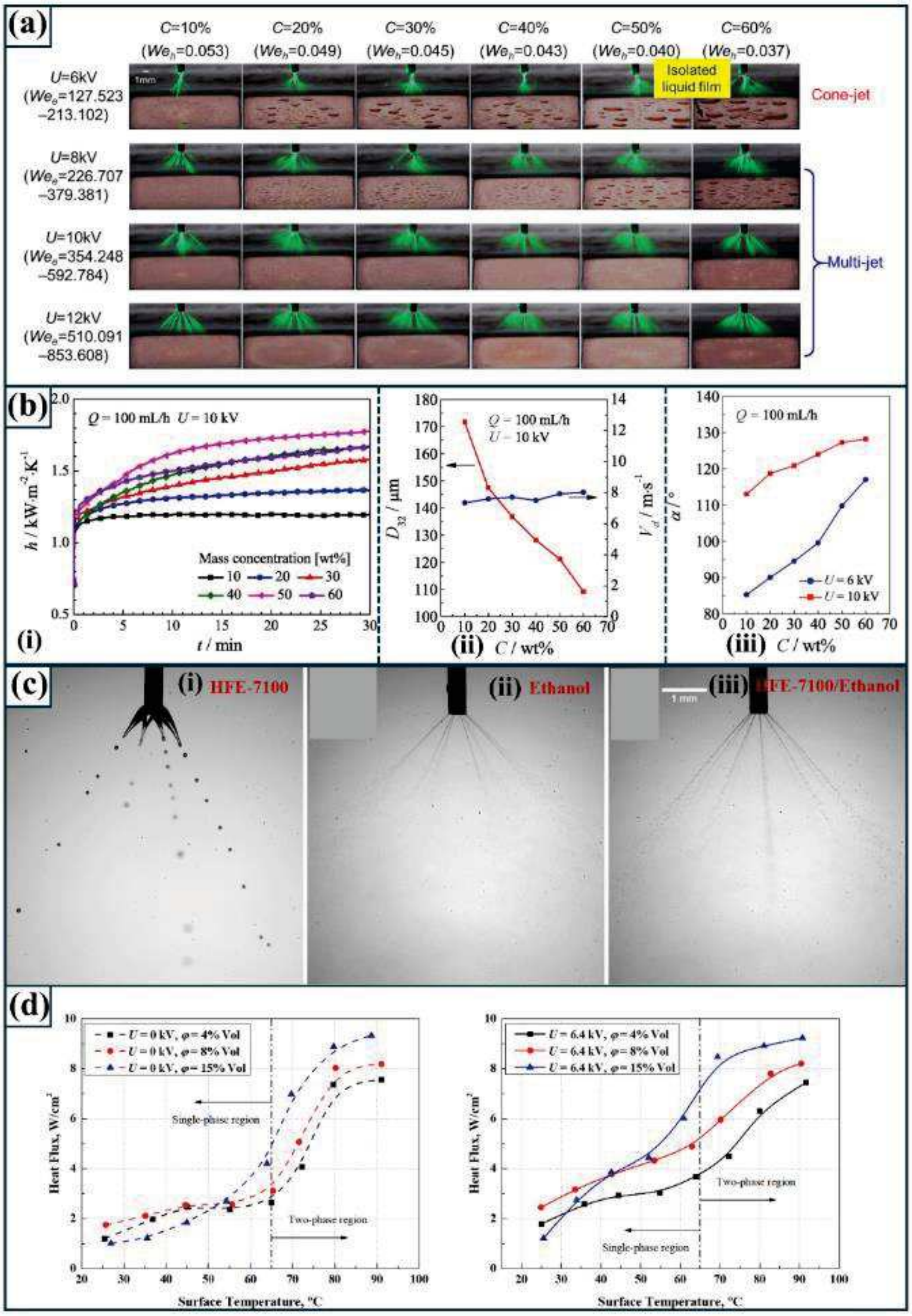

Fig. 8. Electrospray cooling characteristics of dielectric working fluids and mixtures. (a) Electrospray morphologies of ethanol/R141b mixtures at a constant volumetric flow rate of 100 mL/h under different applied voltages and ethanol mass concentrations. Reprinted from Ref. [35] with permission from Elsevier (License No. 6194280714176); (b) Effects of ethanol mass concentration in ethanol/R141b mixtures on (i) HTC, (ii) Sauter mean diameter and average droplet velocity, and (iii) spray angle. Reprinted from Ref. [35] with permission from Elsevier (License No.

6194280714176); (c) Electrospray morphologies of (i) pure HFE-7100, (ii) pure ethanol, and (iii) an 8 vol% ethanol–92 vol% HFE-7100 mixture at a flow rate of 8 mL/h. Reprinted from Ref. [85] with permission from Elsevier (License No. 6194281377302); (d) Variation of heat flux with surface temperature for ethanol and HFE-7100 mixtures under different ethanol concentrations at a flow rate of 100 mL/h. Reprinted from Ref. [85] with permission from Elsevier (License No. 6194281377302).

Regarding the regulation of atomization morphology, the addition of nanoparticles significantly alters the electrical conductivity (K) and surface tension (σ) of the fluid, thereby affecting the stability of the electrospray. Dai et al. [114] showed by molecular dynamics simulations that dilute nanoparticles enhance liquid polarization under an electric field and disrupt the hydrogen-bond network, thereby reducing surface tension and promoting Taylor-cone formation and jet refinement (Fig. 9(a)). However, excessive particle loading increases suspension viscosity and promotes agglomeration, which may destabilize the cone-jet mode and induce irregular multi-jet emission [107,114].

To address the bottleneck of sensible heat capacity, Wan et al. [115] introduced Microencapsulated Phase Change Material Slurries (MPCMS) to leverage latent heat for cooling enhancement. They concluded that under low-temperature conditions (<70 °C), MPCMS significantly outperforms the pure base fluid by virtue of phase-change heat absorption. However, under high-temperature conditions, the deposition layer of microcapsules on the wall increases contact thermal resistance, thereby impairing heat transfer performance (**Fig. 9(b)**). This reflects a common challenge faced by nanofluids in electrospray cooling: unlike traditional large-aperture pressure sprays [116,117], ESC relies heavily on fine nozzle orifices and a strong electric field environment. Consequently, nozzle clogging, the risk of electric breakdown, and mode instability induced by high viscosity upon particle addition have become core bottlenecks limiting its widespread application [107,116]. In contrast, nanofluids have been more extensively investigated in traditional spray cooling due to the larger nozzle scales involved [116,117].

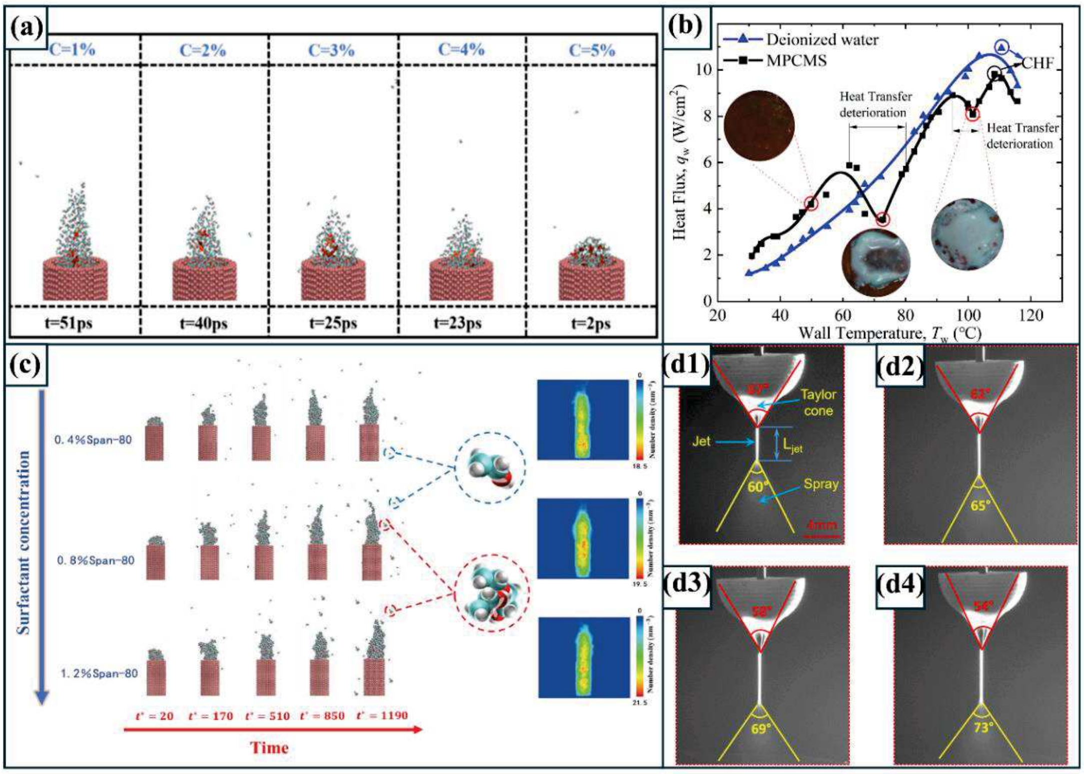

Fig. 9. Effects of nanoparticles and surfactants on electrospray cooling. (a) Effect of different nanoparticle concentrations on the appearance time of the Taylor cone simulated by molecular dynamics. Reprinted with permission from Ref. [114] Copyright 2024 AIP Publishing; (b) Comparison of heat transfer characteristics between microencapsulated phase change material slurry (MPCMS) and deionized water. Reprinted from Ref. [115] with permission from Elsevier (License No. 6194301479646); (c) Electrospray morphology and number-density distributions under different Span-80 concentrations investigated via molecular dynamics (MD) simulation. Reprinted from Ref. [118] with permission from Elsevier (License No. 6194310257530); (d) Photographs of electrospray with "DI water-Triton X-100-ethanol" aqueous working fluid varying with coolant flow rate: (d1) 40 mL/h (Re =20±0.2), (d2) 60 mL/h (Re =30±0.2), (d3) 80 mL/h (Re =40±0.2), and (d4) 90 mL/h (Re =45±0.2), at a constant applied voltage of 12 kV (Bo_E =9.36±0.6). Reprinted from Ref. [119] with permission from Elsevier (License No. 6194310560620).

Surfactants provide a novel approach for modulating electrospray cooling by reducing surface tension and altering charge distribution. These changes influence

Taylor cone formation, droplet size, and surface wettability, thereby enhancing atomization stability and heat transfer. Molecular dynamics (MD) simulations by Li et al. [118] (**Fig. 9(c)**) revealed that surfactant molecules align at the gas-liquid interface, disrupting the solvent's hydrogen bond network and forming 'spindle-like clusters.' This molecular reorganization lowers the energy barrier for jet breakup, facilitating finer droplet generation.

Macroscopically, Ranjan et al. [119] confirmed that non-ionic surfactants (e.g., Triton X-100) improve wettability and broaden the stable voltage window for the cone-jet mode, expanding the spray coverage area (**Fig. 9(d)**). Consequently, the modified coolant achieved a CHF and HTC three times higher than pure water, effectively overcoming the atomization bottleneck of high-surface-tension fluids.

In contrast, research on surfactants in conventional spray cooling is already extensive, encompassing diverse schemes that include traditional surfactants [120], high-alcohol surfactants [121], bio-surfactants [122], and synergistic applications with nanoparticles [123]. It is generally established that an optimal concentration of surfactants enhance both nucleate boiling and CHF performance. This is achieved by lowering surface tension, improving wettability, and modulating droplet Sauter Mean Diameter and liquid film morphology. Therefore, future research necessitates the systematic introduction of these surfactant systems into the ESC framework. Further exploration is required regarding their impact on spray structure, liquid film dynamics, and CHF enhancement potential within the stable cone-jet mode, particularly by integrating the analysis with coupled electric field-flow-heat transfer mechanisms.

Overall, coolant formulation regulates ESC performance by coupling charge relaxation, atomization stability, liquid-film renewal, rewetting, evaporation, and CHF. Appropriate additives can improve droplet spreading and wall-side liquid replenishment, whereas excessive additive loading, particle deposition, viscosity increase, and nozzle clogging may destabilize the spray and weaken phase-change heat transfer.

5.2 Enhanced Electrospray Cooling via Spray Parameter Control

5.2.1 Impact of Voltage and Flow Rate on Electrospray Cooling Performance

In ESC, the applied voltage and liquid flow rate are strongly coupled because they jointly determine spray morphology, liquid replenishment, and CHF. Increasing the flow rate generally increases the number of droplets delivered to the heated surface, thereby improving liquid supply, maintaining film continuity, suppressing local dry-out, and extending the nucleate-boiling regime [87]. Jowkar et al. [124] and Taheri et al. [96] showed that sufficient liquid replenishment enhances total heat removal, and Taheri et al. [96] reported that increasing the flow rate of a water–ethanol mixture from 40 to 80 mL/h increased CHF by approximately 70%. However, the benefit of increasing flow rate is not unlimited. At excessive flow rates, larger jet and droplet diameters can promote thick liquid-film accumulation, increase conductive thermal resistance, and reduce evaporation efficiency. Tian et al. [35] further showed that when the flow rate exceeded 150 mL/h, excessive liquid inertia disrupted atomization stability, generated irregular liquid filaments near the nozzle, and eventually reduced cooling performance through liquid-film flooding.

The applied voltage affects ESC performance mainly by regulating spray morphology and charged-droplet characteristics. As voltage increases, the surface charge density and electric stress acting on the liquid column or filament increase, driving the transition from micro-dripping or columnar emission to stable cone-jet or multi-jet modes. This transition reduces droplet size, increases droplet velocity, and enlarges the spray angle, thereby improving heated-surface coverage and increasing the wetting and evaporation area. As a result, the average HTC is enhanced, especially in the single-phase evaporation and transition regions. Xu et al. [85] reported that, compared with low-voltage columnar flow, the stable liquid sheet and fine droplets induced by high-voltage plume breakup increased the HTC by 2.2 times (**Fig.11(b)**). However, excessive voltage may drive the spray beyond the stable cone-jet or multi-jet window, causing over-dispersion, reducing the effective incident flux, and increasing the risk of corona discharge.

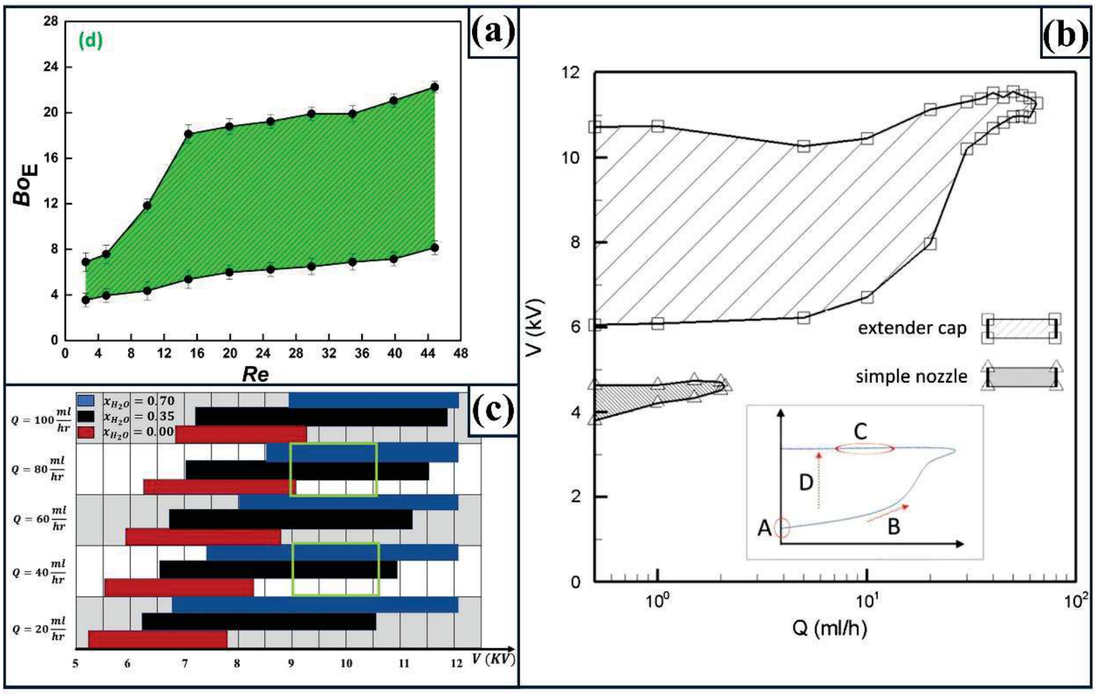

Fig. 10. Cone-jet operating windows under different electric forcing, flow rates, nozzle geometries, and working-fluid compositions. (a) Stability region of cone-jet stability region of an aqueous surfactant solution in the $Re-Bo_E$ plane. Reprinted from Ref. [119] with permission from Elsevier (License No. 6194310560620); (b) Cone-jet stability regions for simple nozzles and nozzles with hemispherical extension caps, using pure ethanol as the working fluid [125]; (c) Cone-jet stability regions for liquids with water volume fractions of 0%, 35%, and 70%. Reprinted from Ref. [96] with permission from Elsevier (License No. 6194311450315).

Flow rate and applied voltage should therefore be considered as coupled control parameters rather than independent variables. The operating map developed by Taheri et al. [96] (**Fig. 10(c)**) quantifies this coupling: the stable cone-jet region systematically shifts toward higher voltages as the flow rate increases. Physically, a higher flow rate requires stronger normal electric stress to balance capillary pressure and stronger tangential electric stress to accelerate the increased liquid momentum. Without a corresponding voltage increase, the spray may degrade into coarse dripping or enter an unstable regime [119].

The stable cone-jet window can be further modified by fluid formulation and nozzle geometry. Ranjan et al. [119] demonstrated that adding a non-ionic surfactant broadened the stable voltage window by reducing surface tension and improving spray coverage (**Fig. 10(a)**). Similarly, Morad et al. [125] showed that extender-cap nozzles expanded the operating range and improved jet steadiness compared with simple capillary nozzles (**Fig. 10(b)**). These operating maps indicate that the stable cone-jet mode should be understood as a parameter-dependent window rather than a single universal threshold. In the representative studies summarized in **Fig. 10**, the cone-jet stability region generally appears within $Bo_E \approx 4-22$ and $Re \approx 1-45$, or within an applied-voltage range of approximately 6–12 kV under cooling-relevant flow rates. However, these numerical ranges are not universal because they depend on liquid properties, nozzle geometry, electrode spacing, and the definition of the characteristic electric field. As the flow rate increases, the stable cone-jet window shifts toward higher voltages, while optimized nozzle structures and surfactant-modified liquids can broaden this window and maintain stable atomization at higher flow rates.

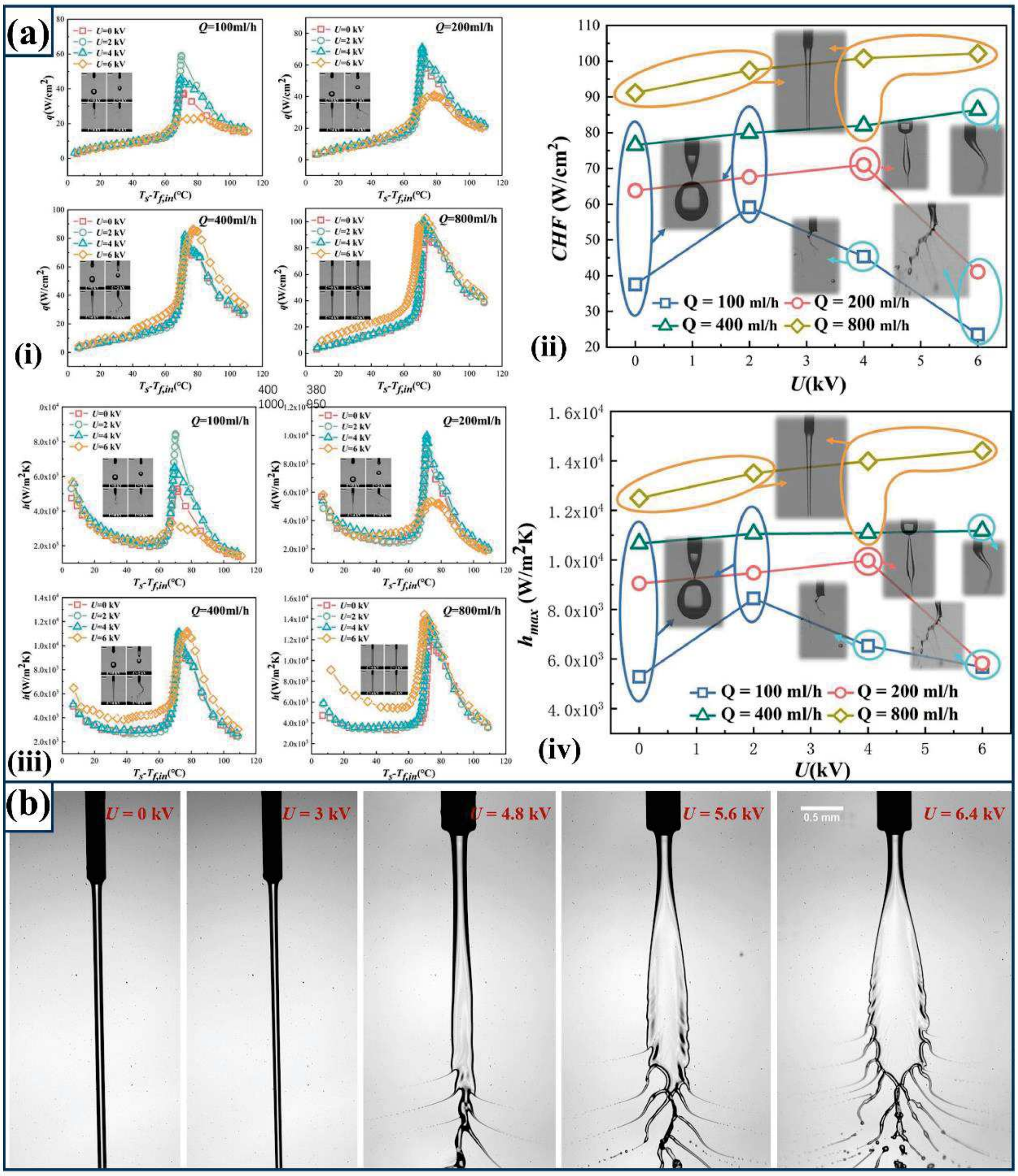

Fig. 11. Effects of applied voltage and flow rate on heat-transfer performance and spray morphology in ESC. (a) (i) Variation of heat flux with superheat under different applied voltages; (ii) variation of CHF under different applied voltages; (iii) variation of HTC with superheat under different applied voltages; (iv) variation of maximum HTC under different applied voltages. Reprinted from Ref. [27] with permission from Elsevier (License No. 6194311097050); (b) Effect of voltage on ethanol and HFE-7100 mixture at a flow rate of 100 mL/h. Reprinted from Ref. [85] with permission from Elsevier (License No. 6194281377302);

High-flow visualization experiments by Shao et al. [27] further established the mapping relationship between spray modes and heat transfer gains (**Fig. 11(a)**): the influence of applied voltage on heat transfer performance is dual-natured and highly dependent on the flow rate and resulting spray morphology. Within the stable jet regime, raising the voltage boosts both heat flux density and CHF. This improvement stems from stronger agitation within the liquid film, which facilitates better coolant spreading. At a flow rate of 800 mL/h and an applied voltage of 6 kV, the CHF reached 100.8 W/cm^2 and the maximum HTC reached 14416.55 $W/(m^2 \cdot K)$. Conversely, pushing the voltage beyond a limit induces jet oscillation. These violent fluctuations splash coolant away from the heater, wasting the liquid. This coolant waste results in an unsustainable liquid film and a subsequent decline in both CHF and the h_{max}, particularly at high flow rates.

Therefore, analyzing the combined effects of voltage and flow rate within a unified framework is key to understanding the intrinsic control mechanism of electrospray cooling. The core law can be summarized as follows: flow rate determines liquid supply and inertia, voltage determines interfacial electric field and atomization intensity, and their coupling ultimately dictates the spray mode, thereby governing the cooling performance to a significant extent.

5.2.2 Impact of Nozzle Parameters on Electrospray Cooling Performance

The nozzle inner diameter serves as a critical geometric parameter governing electric field distribution and spray mode stability; its selection often necessitates a trade-off between operational stability and atomization quality. Kim et al. [78] demonstrated that appropriately increasing the nozzle diameter facilitates the maintenance of a stable cone-jet mode over a wider voltage range, thereby significantly enhancing system operational robustness (**Fig. 12(a)**). Conversely, reducing the diameter offers distinct advantages. Yakut et al. [126] compared nozzle performance ranging from 20 to 26G (inner diameter ~0.9–0.26 mm) and found that reducing the orifice size serves to concentrate the electric field near the tip. This amplification strengthens the electrostatic squeezing effect on droplets. This strong field effect increases average droplet velocity and reduces particle size, which is more favorable for enhancing microscopic heat transfer (**Fig. 12(b)**).

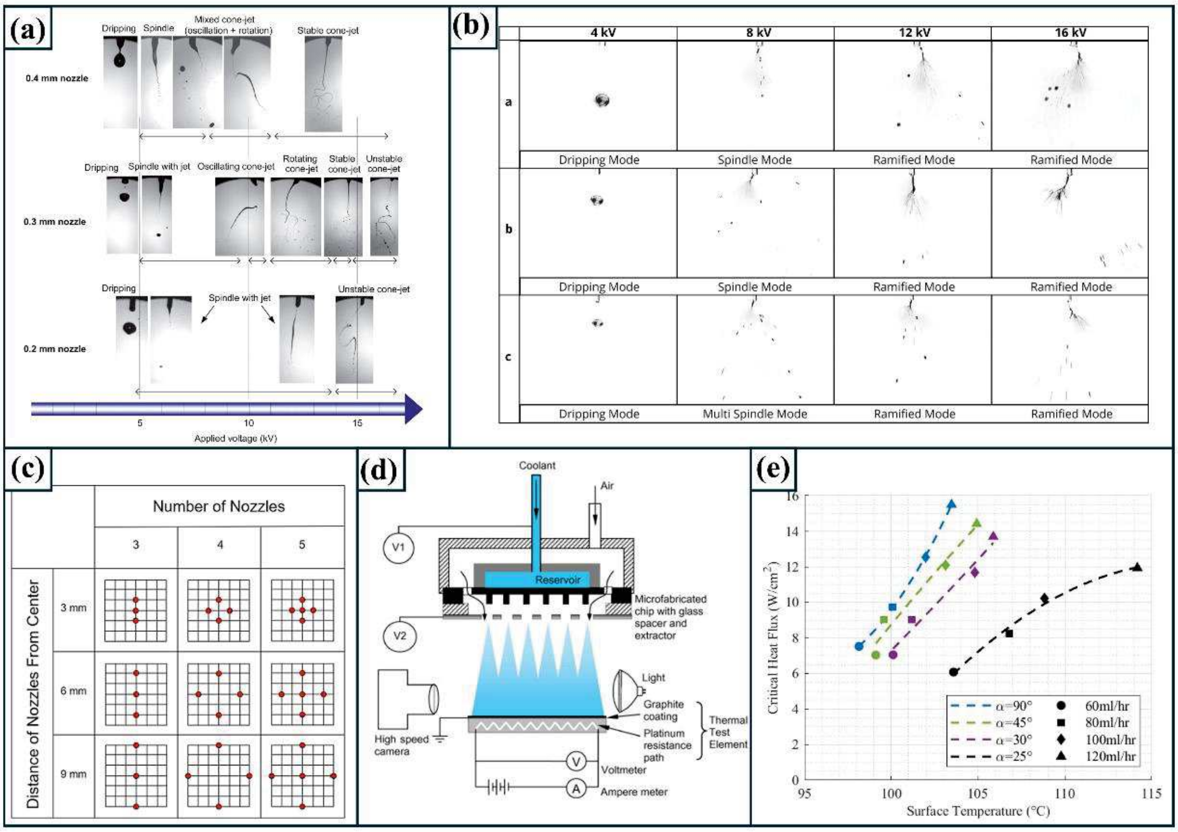

Fig. 12. Effects of nozzle quantity, diameter, and angle on electrospray cooling. (a) Effect of nozzle diameter on spray modes. Reprinted from Ref. [78] with permission from Elsevier (License No. 6194280109434); (b) Electrospray modes under different voltages and nozzle diameters (a: 20G, b: 22G, c: 26G) at a volumetric flow rate of 0.15 mL/min and a nozzle length of 6.35 mm. Reprinted from Ref. [126] with permission from Elsevier (License No. 6194320425190); (c) Positions of capillary nozzles in different combinations on PEEK material. Reprinted from Ref. [82] with permission from Elsevier (License No. 6194320655283); (d) Experimental setup for microfabricated multiplexed electrospray (MES) cooling. Reprinted from Ref. [24] with permission from Elsevier (License No. 6194320901776); (e) Variation of CHF with surface temperature under different flow rates and spray angles. Reprinted from Ref. [127] with permission from Elsevier (License No. 6194321167189).

To leverage the high electric field intensity and heat transfer performance associated with small nozzle diameters, the operating flow rate of a single nozzle is inherently limited; therefore, multi-nozzle or array configurations should be employed to augment total heat removal from the surface. Research by Yakut [82] on multi-nozzle electrospray cooling systems indicates that a configuration of three 26G nozzles (inner diameter ~0.26 mm) with center distance of 5mm yields the highest HTC (**Fig. 12(c)**). To further transcend dimensional limits, Deng and Gomez [24] developed a multiplexed electrospray array with a nozzle outlet diameter of 10 μm and a pitch of 500 μm. Through a Micro-Multiplexed Electrospray (MES) device, stable cone-jet modes generated charged droplets, forming highly efficient evaporative cooling on the chip surface. The experiment achieved a heat flux removal capacity of 96 W/cm^2 and a cooling efficiency of 97% (**Fig. 12(d)**).

Boston et al. [127] confirmed the exceptional adaptability of electrospray to injection angles. Unlike traditional sprays that rely heavily on perpendicular impact, electrospray maintains nominal evaporation efficiencies approaching or even exceeding 100% across a wide inclination range of 30°–90°, with only minor degradation observed at acute angles (25°). This robustness under non-vertical conditions renders it particularly suitable for thermal management applications in spatially confined environments or on complex geometric surfaces (**Fig. 12(e)**).

The geometric configuration of the nozzle determines the local electric field distribution, thereby profoundly influencing the mode evolution and heat transfer performance of the electrospray. Morad et al. [125] first proposed adding a hemispherical cap to conventional nozzles, demonstrating that this structure significantly extends the stability margin of the Taylor cone-jet. Wang et al. [94] systematically compared three geometries—common tube, sheathed tube, and hemispherical tube—and found that the hemispherical geometry homogenizes the electric field at the nozzle exit and mitigates the high-field concentration effect at the tip (**Fig. 13(a)**). Consequently, it facilitates a highly stable and reproducible cone-jet mode. Building on this, Jowkar et al. [124] compared the cooling performance of simple nozzles versus hemispherical nozzles (**Fig. 13(b)**). At flow rates of 40–80 mL/h, simple nozzles tended to produce unstable multi-jet modes with excessive spray coverage, leading to dispersed flux; in contrast, hemispherical nozzles maintained a stable single cone-jet, enhancing cooling efficiency by 40%–75%. To further expand the flow limit, Rahnama et al. [128] developed a porous hemispherical extender (**Fig. 13(c)**). Research indicated that the surface porosity optimizes charge accumulation and liquid supply paths at the interface, significantly widening the cone-jet operating window from 100 mL/h to 250 mL/h, while simultaneously improving CHF and overall cooling efficiency.

From a physical perspective, these macroscopic performance differences stem from the force balance mechanism at the nozzle exit. The evolution of the liquid meniscus is governed by the interplay of Maxwell electric stress, capillary pressure, viscous resistance, gravity, and liquid-supply constraints [77]. For traditional capillary nozzles (as shown in **Fig. 13(d)**), under a strong electric field, the normal electric stress exceeds the capillary restoring stress and stretches the meniscus axially, stretching the meniscus axially. Simultaneously, the tangential electric stress drives the accumulated free ions toward the cone tip, dragging the fluid via viscous action and establishing significant convection and conduction loops within the liquid cone. This mechanism requires the electric stress to remain within a finite stability window determined by capillary pressure, viscous resistance, charge relaxation, and liquid supply [74]. In contrast, nozzles with hemispherical caps or special geometric modifications exhibit distinct stress distribution characteristics (as shown in **Fig. 13(e)**). In addition to normal and tangential electric stresses, the polarization contribution to the interfacial electric stress can assist the initial meniscus deformation. Since the hemispherical geometry provides a stable initial physical curvature, this structure effectively modulates the electric field gradient near the nozzle, enhancing the electric traction and interfacial electric traction and charge-induced repulsion on the fluid. This facilitates the jet in overcoming the constraints of surface tension and viscous resistance to achieve atomization [96,124].

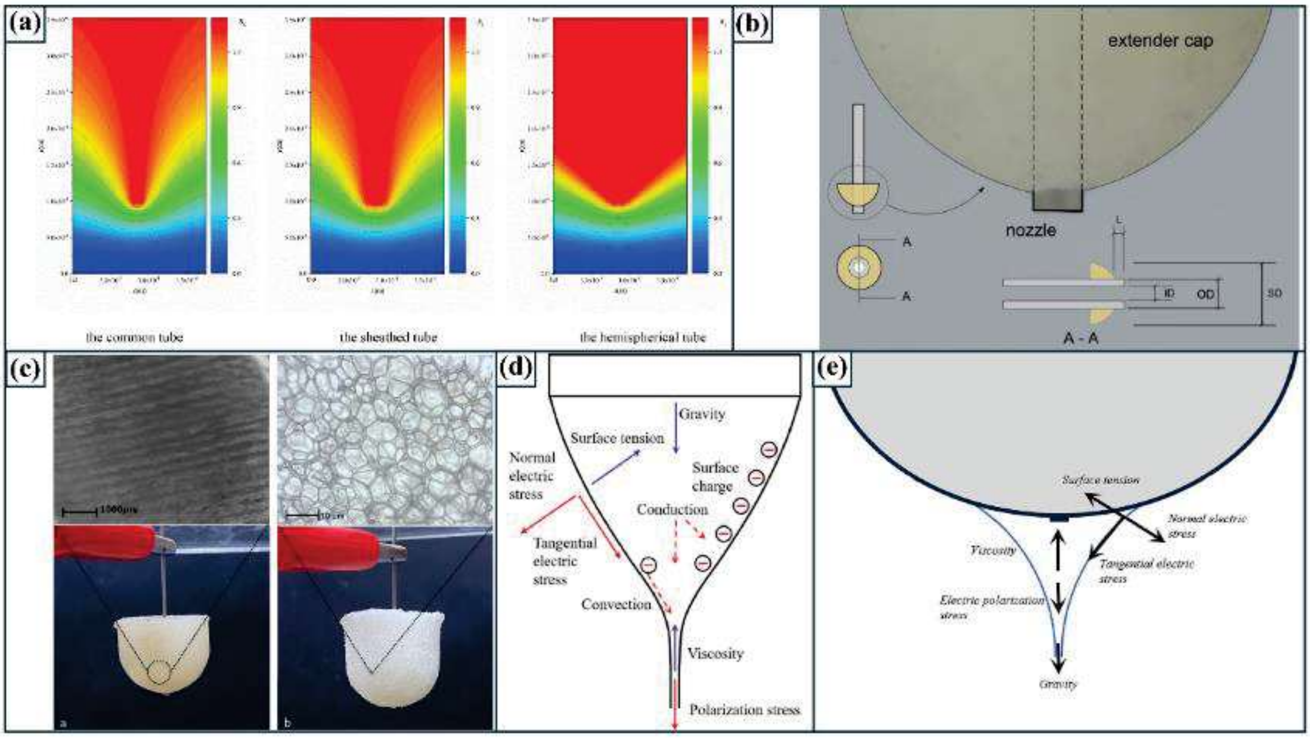

Fig. 13. Effects of nozzle geometry and extender design on electric-field distribution and liquid-meniscus force balance in electrospray. (a) Electric-field distributions near common, sheathed, and hemispherical tubes. Reprinted from Ref. [94] with permission from Elsevier (License No. 6194300208596); (b) Geometry of the hemispherical extender-cap nozzle [124]. (c) Two types of extenders installed at the nozzle tip: an impermeable solid surface and a porous surface (polyurethane). Reprinted with permission from Ref. [128]. Copyright 2025 AIP Publishing. (d) Force balance on the liquid meniscus of a conventional capillary nozzle. Reprinted from Ref. [94] with permission from Elsevier (License No. 6194300208596); (e) Force balance on the liquid meniscus of a nozzle modified with a hemispherical extension cap. Reprinted from Ref. [96] with permission from Elsevier (License No. 6194311450315).

5.3 Enhanced Electrospray Cooling via Surface Modification

5.3.1 Phase Change Enhancement Mechanisms Based on Surface Microstructures

Preceding sections investigated the regulatory effects of electrospray morphology, dielectric properties, and spray parameters on cooling performance. Upon droplet impact on the heated surface, complex dynamic and thermodynamic processes ensue, including droplet spreading, bubble nucleation and departure, liquid film evaporation, and surface rewetting. Consequently, a core strategy for enhancing cooling lies in intervening in these processes via surface modification: employing macroscopic structures to expand the effective heat exchange surface and promote film disturbance. Additionally, micro/nano-structures is employed to boost wettability, multiply nucleation sites, and intensify capillary wicking capabilities. Research on surface microstructures in traditional spray cooling is well-established, spanning from macroscopic micro-fins (e.g., straight and cubic fins) to micro/nano-porous coatings and copper micromeshes, and extending to ordered hierarchical structures designed for vapor-liquid separation.

At the macroscopic dimension, micro-fins improve thermal performance mainly by enlarging the solid-liquid contact interface between the liquid film and the heat sink, extending the length of the Three-Phase Contact Line (CLL), and regulating liquid film distribution [129,130]. The effects of different fin geometries on surface heat flux are illustrated in **Fig. 14(a)**. Salman et al. [131] conducted comparative experiments on various macroscopic structures within a spray cooling system. Results indicated that under identical operating conditions, the optimized M3 surface (featuring complex geometric fin characteristics) achieved a 34% increase in heat dissipation capacity compared to a traditional straight-groove modified surface, attributed to its effective guidance of liquid film flow and area extension (**Fig. 14(b)**).

Unlike macroscopic structures, micro/nano-coatings and porous surfaces enhance microscopic phase-change processes mainly by altering surface energy and pore structure. These structures not only significantly improve surface wettability—utilizing capillary wicking to accelerate liquid spreading and rewetting—but also provide a multitude of potential bubble nucleation sites, thereby significantly augmenting nucleate boiling. Bostanci et al. [132] evaluated Electroplated Microporous Surfaces (EMS), Sanded Surfaces (SS), Bead-blasted Surfaces (BS), and Reference Smooth

Surfaces (RS) using HFC-134a and HFO-1234yf refrigerants. They found that the EMS surface achieved the highest heat transfer enhancement ratio due to its rich microporous structure (**Fig. 14(c)**). Similarly, Kim et al. [133] observed in ultra-low flow rate (0.0012 mL/($cm^2 \cdot s$)) water spray experiments that microporous aluminum coatings (<200 μm) (**Fig. 14(d)**)generated strong capillary wicking effects through interconnected internal micro-cavities. This effectively prevented local dry spot formation, increasing CHF by 40% compared to smooth surfaces. Thiagarajan et al. [134] reached similar enhancement conclusions in spray boiling experiments using HFE-7100 on conductive microporous copper surfaces.

The physical nature of the heat transfer enhancement by the aforementioned micro/nano-structures has been confirmed through refined observation experiments. Horacek et al. [135] employed Total Internal Reflection (TIR) techniques for in-situ observation of low-flow spray cooling, successfully capturing the dynamic evolution of the FC-72 liquid film and quantitatively measuring the Three-Phase Contact Line Length (CLL) (**Fig. 14(e)**). The study revealed a critical physical law: the phase-change heat transfer rate exhibits a strict linear relationship with the three-phase CLL. Sodtke and Stephan [136] further corroborated this mechanism using infrared thermography. They pointed out that the fundamental reason micro-cone or micro-pore structures significantly enhance performance is that their porous topology permits liquid film permeation, thereby drastically extending the effective length of the three-phase contact line (**Fig. 14(f)**). Concurrently, the synergistic effect of the large specific surface area and capillary wicking capability of microporous coatings ensures that droplets are rapidly absorbed and diffused at low flow rates, maximizing coolant evaporation utilization and overall heat transfer capacity.

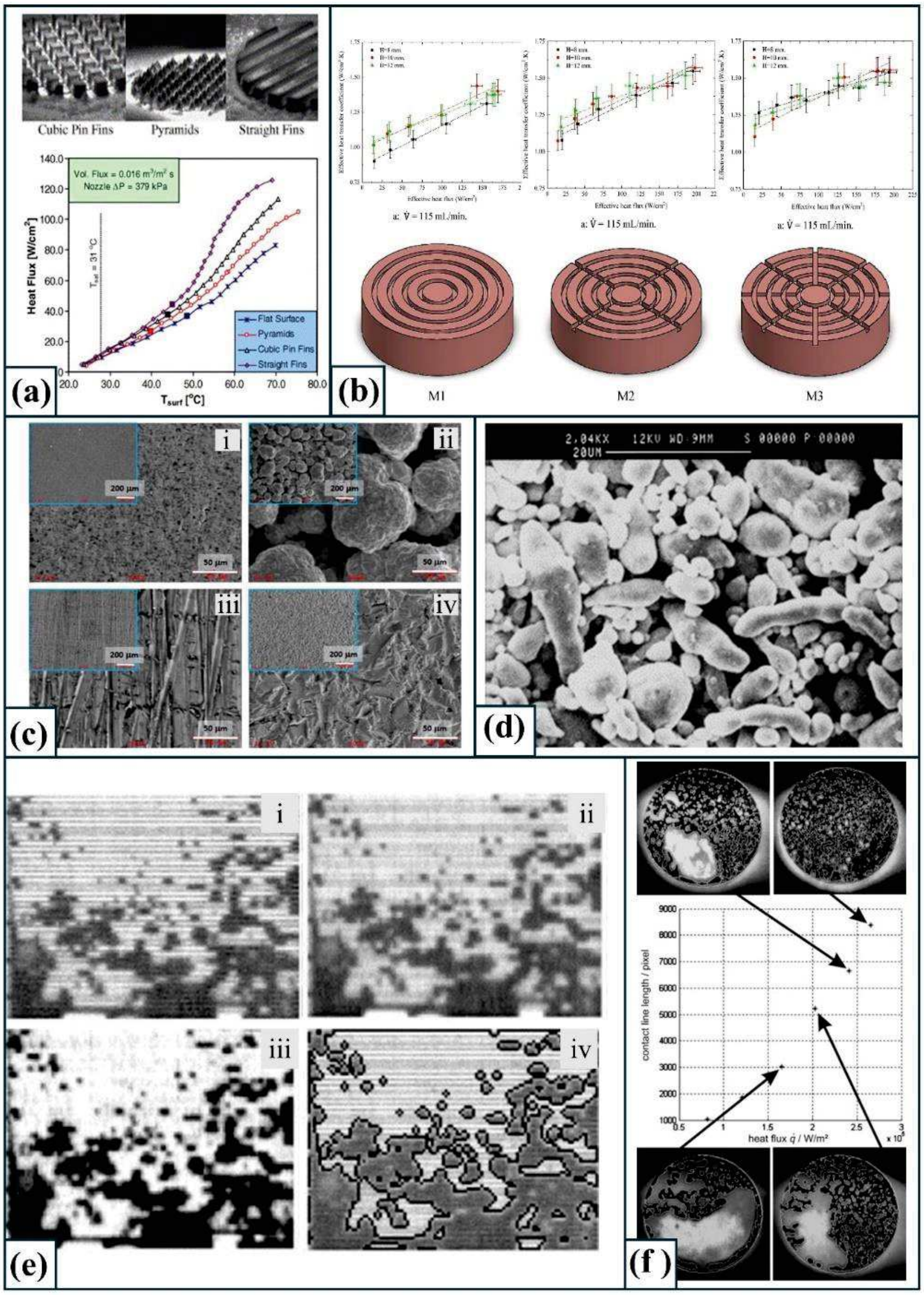

Fig. 14. Effects of surface microstructures on conventional spray cooling. (a) Images of square pin fin, pyramid, and straight fin enhanced surfaces, and plots of heat flux versus surface temperature. Reprinted from Ref. [129] with permission from Elsevier (License No. 6194331448190); (b) CAD images of M1, M2, and M3 structured surfaces, and the effect of nozzle-to-surface distance on effective heat flux for M1, M2, and M3 surfaces at a flow rate of 115 mL/min.

Reprinted from Ref. [131] with permission from Elsevier (License No. 6194340307346); (c) SEM images of surfaces: (i) RS, (ii) EMS, (iii) SS, and (iv) BS at 100x and 500x magnifications. Reprinted from Ref. [132] with permission from Elsevier (License No. 6194340541760); (d) SEM image of the ABM coating. Reprinted from Ref. [133] with permission from Elsevier (License No. 6194340729030); (e) Image processing sequence: (i) raw image, (ii) application of a 2-pixel orthogonal filter, (iii) row-by-row renormalization, and (iv) final detected edges superimposed on the raw image. Reprinted from Ref. [135] with permission from Elsevier (License No. 6194341039305); (f) Contact line length versus heat flux and corresponding infrared images. Reprinted from Ref. [136] with permission from Elsevier (License No. 6194341240862).

However, excessively dense, disordered, or overly thick microporous structures can precipitate the premature onset of the LFP. The resulting severe liquid-vapor counterflow impedes vapor escape while simultaneously obstructing droplet permeation and liquid rewetting. Hu et al. [137] explored thermal enhancement techniques using copper micromesh surfaces. They observed that although increasing the number of mesh layers shortened liquid permeation time and multiplied nucleation sites, heat transfer performance deteriorated when the thickness exceeded three layers. This decline was attributed to trapped vapor, which hindered further droplet infiltration and rewetting (**Fig. 15(a)**).

To overcome this bottleneck, Jiang et al. [138] pioneered a Structure for Suppressing the Leidenfrost Effect (STA) (**Fig. 15(b)**). The core concept involves constructing dedicated U-shaped vapor venting channels to achieve the spatial separation of liquid and vapor transport paths. This design philosophy of "vapor-liquid separation" was subsequently introduced into the spray cooling domain to address vapor resistance issues under high heat flux conditions.

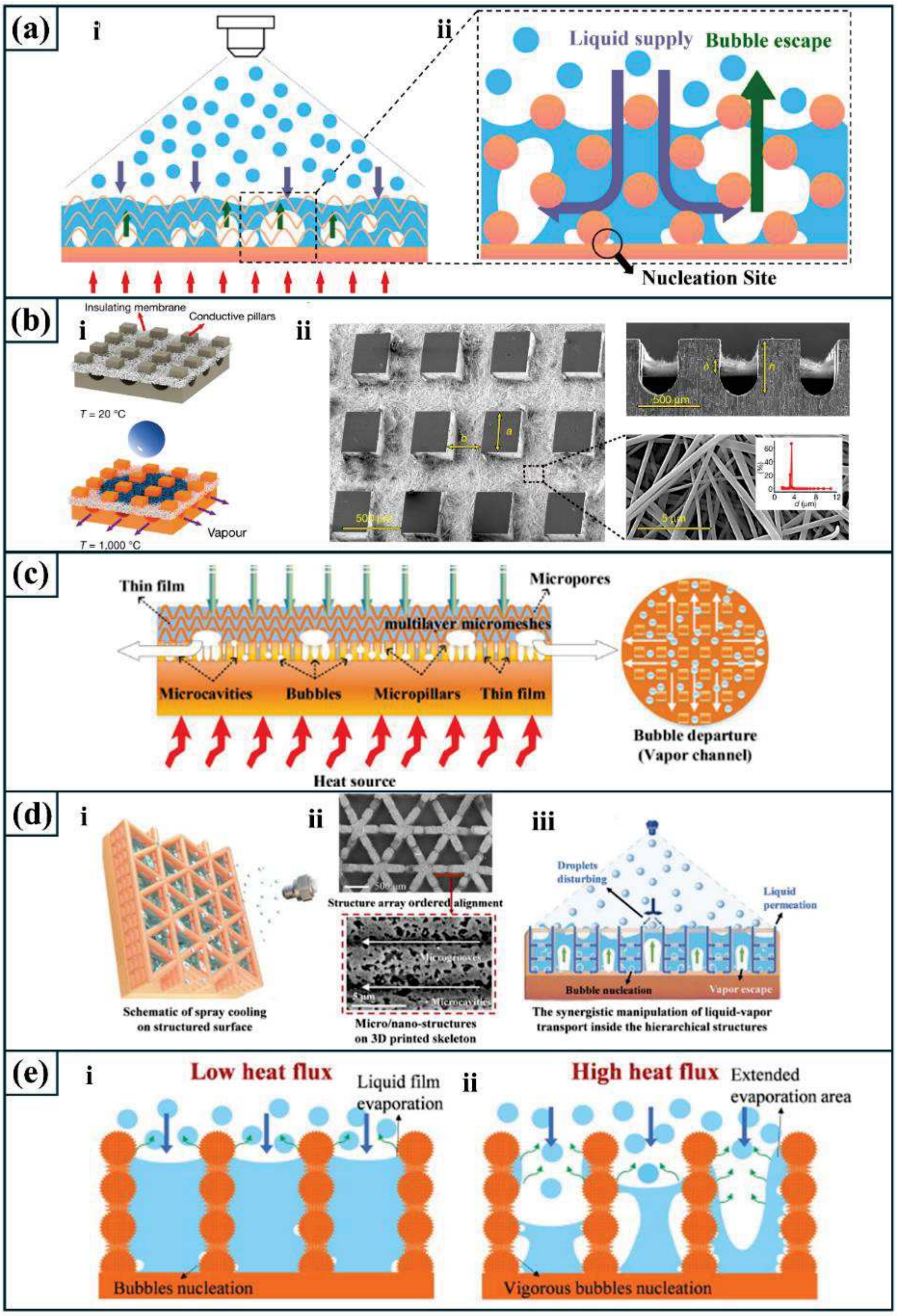

Fig. 15. Hierarchical and multilayer surface structures for regulating liquid–vapor transport in spray cooling.(a) Blocking effect of vapor bubbles on droplets on the multi-layer copper micromesh surface. Reprinted from Ref. [137] with permission from Elsevier (License No. 6194350177985); (b) Structure for suppressing the Leidenfrost effect (STA): composed of thermal conductive pillars, a liquid-wicking insulating membrane, and dedicated vapor venting channels. Reprinted by permission from Springer Nature: Nature Ref. [138], copyright (2022); (c) Double-layer surface structure achieving vapor-liquid separation. Reprinted from Ref. [139]with permission

from Elsevier (License No. 6194350360360); (d) Morphology and schematic of synergistic vapor-liquid transport within a 3D ordered hierarchical micro/nano-structured surface. Reprinted from Ref. [140] with permission from Elsevier (License No. 6194350614102); (e) Mechanism of boiling inversion: at high heat flux, film thinning exposes more structures and activates sidewall nano-cavities, achieving simultaneous enhancement of nucleate boiling and thin-film evaporation. Reprinted from Ref. [140] with permission from Elsevier (License No. 6194350614102).

Ni et al. [139] proposed an innovative dual-layer decoupling surface: the upper copper micromesh facilitates liquid capture and spreading, while the lower micropillar array manages phase-change heat transfer and vapor discharge (**Fig. 15(c)**). This design successfully achieves the functional decoupling of liquid supply and vapor separation. During the single-phase regime, the extended surface area from the surface structures augments convective cooling. With rising heat flux, the primary thermal transport mechanism shifts smoothly to efficient venting through inter-pillar gaps. This effectively prevented bubble coalescence, increasing the HTC by 37.6% and significantly delaying CHF.

Furthermore, by integrating high-precision 3D printing and template-assisted electrodeposition, Hu et al. [140] successfully engineered a three-dimensional ordered hierarchical micro/nano-structure (**Fig. 15(d)**). This structure exhibited a remarkable adaptive enhancement mechanism: as heat flux increased, the receding liquid level exposed more sidewall surfaces, where micro-grooves and nano-cavities were progressively triggered to serve as secondary nucleation sites, thereby sustaining vigorous nucleate boiling (**Fig. 15(e)**). The combined amplification of thin-film evaporation and nucleate boiling enabled an astounding CHF of 1273 W/cm^2 and a HTC of 443.7 $kW/(m^2 \cdot K)$.

Although these complex structures have not yet been widely applied in electrospray cooling, their design philosophy of vapor-liquid separation provides a crucial blueprint for future micro-structure designs in ESC.

5.3.2 Enhanced Electrospray Cooling via Surface Modification

Distinct from the purely thermodynamic enhancements discussed in Section 6.3.1, the introduction of surface structures in electrospray cooling not only alters the heat transfer area but also induces additional Electrohydrodynamic effects. As electrospray cooling is a relatively nascent field, research targeting nano-coatings or microporous surfaces remains in the exploratory stage. Furthermore, complex ordered structures designed for vapor-liquid separation—common in traditional spray cooling—have not yet been developed for ESC; existing surface modification efforts focus primarily on macroscopic fin and grid structures.

In terms of basic surface configurations, Zhang et al. [141] utilized deionized water to evaluate the performance of eight different surfaces, including wire-cut grooves and sandpaper-polished surfaces. They found that grooved surfaces with minimal spacing performed best, demonstrating the guiding role of micro-textures in liquid film spreading. Similarly, Kabakuş et al. [142] introduced different macroscopic fins (**Fig. 16(a)**) to the cooling surface; although the electrospray mode remained unaltered by the macro-structure, cooling performance improved by 1.3–1.6 times compared to smooth plates, primarily attributed to the increased surface area. Regarding experimental design and optimization, Yakut [143] applied Response Surface Methodology (RSM) to optimize lattice fin heat sinks, achieving a performance improvement of up to 20% compared to flat plates. Subsequently, Kabakuş and Yakut [144] employed the Full Factorial Method and determined that a square heat sink configuration with specific dimensions (width, spacing, and height all set to 3 mm) yielded the optimal cooling effect.

Tian et al. [145] experimentally investigated the influence of four different macroscopic structured copper surfaces (**Fig. 16(b)**)on the dynamics and cooling performance of ethanol electrospray. They simulated the electric field distributions of five surfaces (**Fig. 16(c)**) and defined an area ratio f, to evaluate the cooling performance improvements achieved through surface modification.

$$f = A_s / A_b \tag{17}$$

Here, A_b and A_s refer to the flat substrate area and the structured surface area, respectively, while the cumulative heat exchange area is denoted by A_{tot} .Experimental observations reveal that the governing heat transfer mechanisms shift depending on the specific temperature zone. Regarding the low-temperature stage, cooling performance is largely dictated by electric field-driven convection and bubble dynamics. As the surface temperature climbs to the medium range, the presence of macroscopic structures serves to multiply nucleation sites, thereby boosting nucleate boiling. At an applied voltage of 4.5 kV, the critical heat flux density (CHF) of the cubic fin surface is increased by 63% compared to that of the planar surface [145]. However, this structural advantage fades at higher superheats, where the premature onset of the Leidenfrost effect hinders effective liquid-solid contact. This suggests that the enhancement effects of the electric field and the structured surface on electrospray cooling are not independent but rather exhibit a coupling relationship. Furthermore, they found that bubble generation is largely influenced by the fin structure; compared to conical pin fins, cubic pin fins possess a larger surface area and provide more nucleation sites on their tetrahedral structures (**Fig. 16(c)**).

In electrospray cooling, charged droplets are sprayed onto a heated surface. Upon impingement and spreading, droplets form a transient liquid film, which undergoes local boiling and evaporation under continuous replenishment by incident droplets. The interplay involving bubble dynamics and the liquid film is fundamental to the heat transfer mechanism in spray cooling. In particular, the local liquid film thickness governs the superheatand nucleation conditions. Simultaneously, the processes of bubble generation, growth, coalescence, and detachment directly regulate the wetting state and heat transfer intensity of the heat sink surface.

Extensive research indicates that bubbles play a dual role in spray cooling: they serve as both carriers of heat transfer and triggers for surface dry-out and rewetting.

The periodic formation and detachment of bubbles continuously perturb the liquid film. This process renews the boundary layer and enhances convective and phase-change heat transfer. Consequently, bubble dynamics significantly influence the HTC and CHF [146,147].

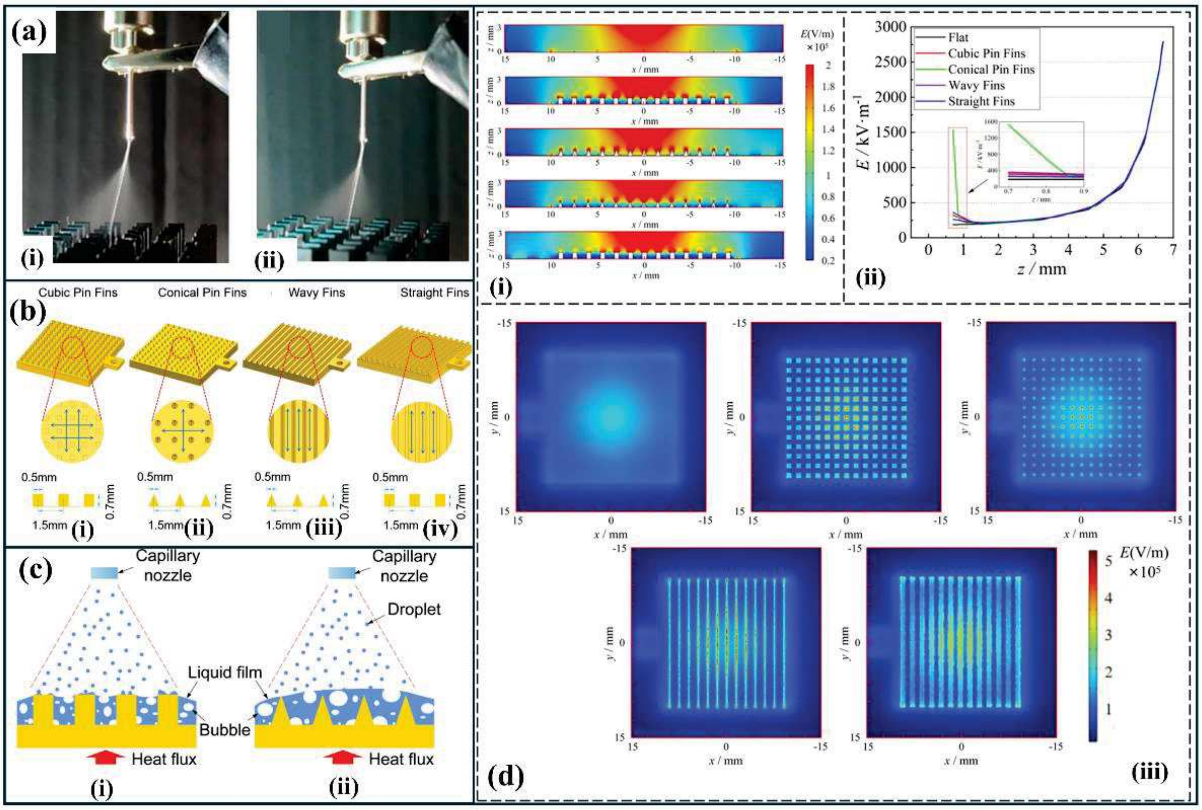

Fig. 16. Enhancement effects of surface modification on electrospray cooling. (a) Electrospray images, with flow rates of (i) 0.45 mL/min and (ii) 0.60 mL/min, respectively. Reprinted from Ref. [142] with permission from Elsevier (License No. 6194351061233); (b) Macro-structures of cooling surfaces: (i) cubic pin fins, (ii) conical pin fins, (iii) wavy fins, and (iv) straight fins. Reprinted from Ref. [145] with permission from Elsevier (License No. 6194351349922); (c) Droplet and bubble behaviors on heated surfaces with (i) cubic pin fins and (ii) conical pin fins. Reprinted from Ref. [145] with permission from Elsevier (License No. 6194351349922); (d) Electric field intensity distributions for different cooling surfaces: (i) electric field intensity on the central x-z plane ($0 \le z \le 3$), (ii) electric field intensity as a function of axial distance, and (iii) electric field intensity distribution on the x-y plane (z = 0.7 mm). Reprinted from Ref. [145] with permission from Elsevier (License No. 6194351349922).

Furthermore, the dielectrophoretic force and polarization effects alter the force distribution at the inner and outer interfaces of bubbles. This causes the bubble morphology to tend from spherical toward elliptical or columnar shapes. Additionally, an additional electric body-force component is generated along the electric-field direction . This driving force increases bubble detachment frequency, shortens residence time, and reduces bubble aggregation. Following bubble detachment, the electric field accelerates the rewetting and liquid replenishment processes of the surrounding liquid. This mitigates the risk of local dry-out [73,148,149].

When employed in conjunction with structured surfaces, a synergistic effect emerges between the electric field and the structure [150]. The combined influence of electric field and structural parameters is not a simple linear addition. This is because the macroscopic surface structure alters the local electric field distribution on the heated wall. Consequently, the dielectrophoretic force acting on the bubbles is intensified. This enhancement alters bubble dynamics, which in turn leads to heat transfer enhancement [146] (**Fig. 17(a)**).

In scenarios characterized by limited coolant flow and moderate heat flux, the system operates primarily in a thin-film boiling regime. Here, impinging droplets create a temporary liquid layer immediately upon contact the heat sink surface. The thickness of the liquid film determines the local superheat and nucleation conditions. The introduction of an electric field plays a distinct role in this process. The electrowetting effect (**Fig. 17(b)**) alters the spreading characteristics and static contact angle following droplet impact. This influences the instantaneous thickness of the liquid film and the bubble nucleation sites [151,152], thereby increasing the length of the three-phase contact line.

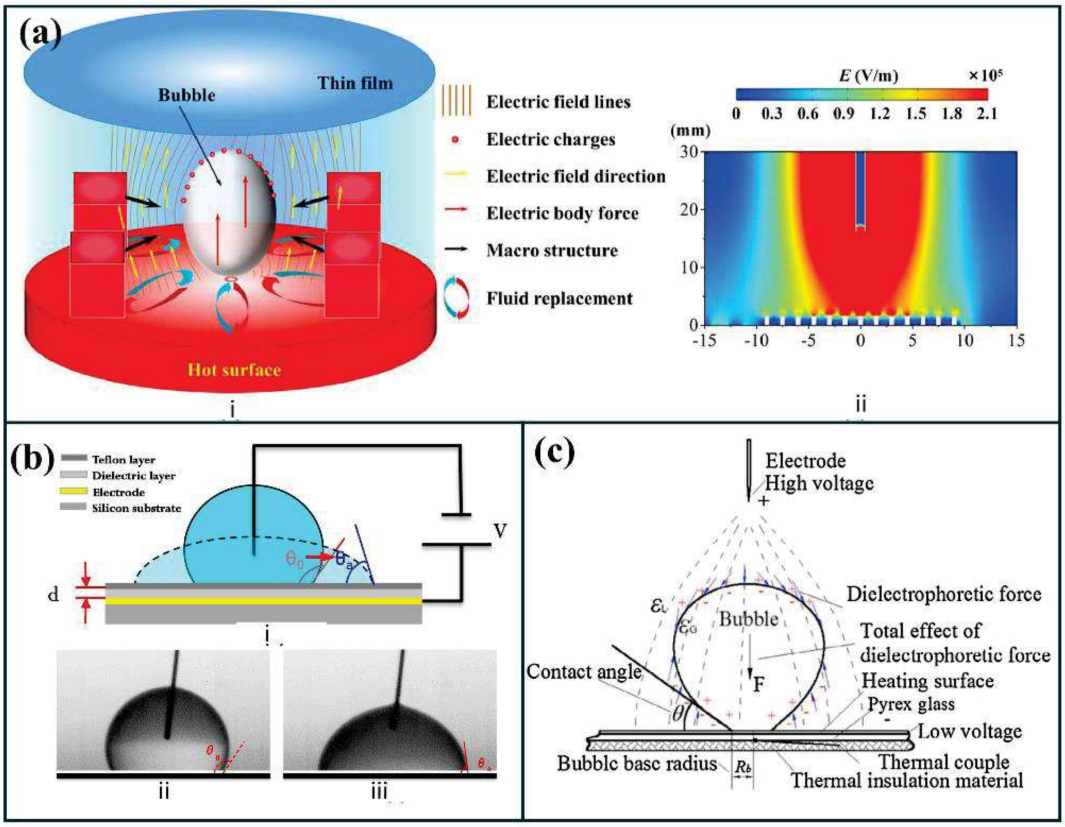

Fig. 16. Influence of electric fields on droplets and bubbles. (a) (i) Schematic diagram of boiling bubble dynamics within a thin film; (ii) Simulated electric field intensity. Reprinted from Ref. [146] with permission from Elsevier (License No. 6194360240269); (b) Electrowetting of a water droplet: (i) Typical electrowetting (EW) setup; (ii) Intrinsic hydrophobic state prior to electrowetting; (iii) Hydrophilic state under the electrowetting effect. Reprinted from Ref. [151] with permission from Elsevier (License No. 6194360468168); (c) Schematic of single bubble growth under the influence of an electric field. Reprinted with permission from Ref. [153] Copyright 2025 AIP Publishing.

In contrast, elevated flow rates and heat fluxes shift the system towards a regime dominated by droplet impact. In this phase, the synergistic effect of surface morphology and electric field more closely resembles a pool boiling mode. In this scenario, droplets not only impact and spread across the heat sink surface but also continuously supply liquid to the surface. This leads to local boiling and evaporation. Increasing the spray volume causes droplets to blanket the heat sink, resulting in a thicker liquid film that facilitates bubble generation, coalescence, and detachment [73,154]. Therefore, in this pool-boiling-like mode, the electric field significantly enhances cooling performance by accelerating bubble detachment and facilitating liquid rewetting (**Fig. 17(c)**).

Overall, surface modification enhances ESC by coupling wall wettability, liquid-film evolution, bubble dynamics, vapor removal, and local electric-field distribution. Fins, grooves, and grid-like structures can improve liquid spreading, increase nucleation-site density, and modify bubble behavior, but their benefits may diminish when vapor accumulation or excessive liquid-film thickness weakens liquid–solid contact. Therefore, ESC surface design should move beyond simple area enlargement toward structures that guide charged-droplet deposition, sustain capillary rewetting, and provide vapor-escape pathways, thereby maintaining stable boiling and delaying dry-out under high heat flux.

6 Dimensionless characterization, heat-transfer correlations, and predictive modeling of electrospray cooling

Classifications based on spray morphology and operating parameters are useful for identifying electrospray regimes, but they do not quantify how a given regime translates into droplet size, liquid-film renewal, boiling intensity, or heat-transfer capacity. Dimensionless analysis is therefore required to reduce the number of governing variables and to express electric forcing, liquid inertia, viscous resistance, capillary effects, phase change, and geometric confinement on common nondimensional scales. In ESC, these parameters are physically connected through the pathway from EHD atomization to interfacial heat transfer. Bo_E and We both use capillary effects as the reference scale, but they quantify different competing mechanisms: Bo_E represents electric stress, whereas We represents liquid inertia. Their combined values describe whether the meniscus and emitted jet are dominated by capillary retention, electric stretching, or inertial jetting, thereby governing spray-mode transition and droplet-scale boundary conditions. Re further incorporates flow-rate-driven liquid supply and viscous resistance, which affect droplet deposition, liquid-film renewal, and surface rewetting. These spray- and film-scale processes determine local wall superheat and phase-change intensity, which are reflected by Ja. Nu is therefore the final thermal response of this coupled electric-field–flow–phase-change pathway. It is important to highlight that the specific formulations of We and Bo_E often vary across the literature. This review utilizes Bo_E and We to represent the electric Bond number and Weber number, respectively, while original numerical parameters from each study are retained.

Table 4: Prediction of droplet diameter and Nusselt number via dimensionless analysis

Reference	Prediction target and dominant process	Correlation / Findings	Applicable range	Fluid	Error	Original notation / definition
Wang et al. [155]	Minimum droplet diameter formula; EHD atomization	$d_{\text{dripping}} = 0.66 \times d_0$ $d_{\text{spindle}} = 0.66 \times 0.24 \times d_0$ $d_{\text{cone-jet}} = 0.66 \times 0.24 \times 0.08 \times d_0$	Flow rate: 20-35 mL/h; Electrode distance :100 & 150 mm	Acetic acid	-	d: droplet diameter; d_0: droplet diameter without electric field; D: nozzle outer diameter
	Formula for decreasing droplet diameter percentage; EHD atomization	$\frac{\left(\frac{d}{D}\right)_{i+1} - \left(\frac{d}{D}\right)_i}{\left(\frac{d}{D}\right)_i} \times 100 = -(49 \times We^{-0.03}) + (35 \times We^{-0.03}) \times \tanh^2\left(1.8 \times \left(1 + \left((0.0086 \times We^{-0.03} \times Ca_e) - 2.5\right)^3\right)\right)$				
Estrada-Díaz et al. [156]	Jet diameter; Taylor cone-jet formation	$\frac{D}{D_0} = \left(\frac{ED_0^3}{Q}\sqrt{\frac{K}{\mu}}\right)^{-0.6888} \times \left(\frac{\sigma D_0^2}{\mu Q}\right)^{0.3166} \times \varepsilon_l^{0.152}$	Flow rate:20-35 mL/h; Voltage:0-3.5 kV	Ethylene glycol and deionized water	4.69%	D: jet diameter; D_0: wetting diameter

Tian et al. [35]	Dimensionless diameter D_{32}; EHD atomization	$\frac{D_{32}}{D_0} = 0.33 \cdot Bo_E^{-0.15} \cdot We^{0.04} \cdot Re^{-0.05}$	Flow rate:100-200 mL/h; Voltage: 6-12 kV	Ethanol–R141b mixture	15%	$Pr=\mu c_l/k_l$: Prandtl number, representing the ratio of momentum diffusivity to thermal diffusivity.
	Nu ; droplet-impact and film-renewal heat transfer	$Nu = 539.15 \cdot Bo_E^{0.13} \cdot We^{0.21} \cdot Pr^{-0.43}$			15%	
Shao et al. [27]	Maximum Nu ;inertia-assisted liquid-film renewal	$Nu_{max} = 706.586 \times We^{0.174} \times Bo_E^{0.042}$	Flow rate:0-800 mL/h; Voltage: 0-6 kV	Anhydrous ethanol	5%	-
Xu et al. [85]	Nu ; droplet impingement and phase-change heat transfer	Single-phase region: $Nu = 85.93 \cdot Re^{0.79} \cdot We^{-0.17} \cdot Pr^{-2.50} \cdot Bo_E^{0.27} \cdot Td^{-0.39}$ Two-phase region: $Nu = 2.68 \cdot Re^{1.10} \cdot We^{-0.13} \cdot Pr^{-1.47} \cdot Bo_E^{0.17} \cdot Td^{-0.69} \cdot Ja^{0.12}$	Flow rate:50-150 mL/h; Voltage:0-6.4 kV	HFE-7100 and ethanol mixture	20%	$T_d=\frac{T_{sur}-T_{liq}}{T_{sat}}$ $Ja=\frac{c_p(T_{sur}-T_{sat})}{h_l}$
Kim et al. [157]	Nu ; boiling-regime-dependent phase-change heat transfer	Single-phase region: $Nu = 9.92 \cdot We^{0.021} \cdot Bo_E^{0.15} (Bo^* < 0.02)$ Transition region: $Nu = 49.0 \cdot Bo^{*0.41} \cdot We^{0.026} \cdot Bo_E^{0.17} (0.02 < Bo^* < 0.024)$	Flow rate: 200-600 μL/min; Voltage: 0-7 kV	Water	20%	B_0^* is the modified boiling number

		Nucleate boiling region: $Nu = 731.96 \cdot Bo^{*0.85} \cdot We^{0.012} (0.024 < \mathrm{Bo}^{*})$				
Wang and Mamishev [158]	Enhancement Ratio (ER) of the ESEC chamber; EHD-enhanced evaporative heat transfer Nu ; confined evaporative heat transfer	$ER = f\left(N, \frac{L^*}{D_i}, Bo_E, We, Re\right) = a \cdot Bo_E^b \cdot We^c \cdot Re^d \cdot \left(\frac{N \cdot L^*}{D_i}\right)^e$ $Nu = aWe_E^b We^c Re_{D_i}^d (N\frac{L^*}{D_i})^e Pr^g$	Flow rate:1-8 cm³/h; Voltage:4-7.7 kV; The values of a, b, c, d, e are related to the nozzle chamber	Ethanol	10%	N is nozzle number; L^*/D_i is a geometry-related length ratio

The correlations summarized in Table 4 show that dimensionless analysis in ESC serves both predictive and diagnostic functions. For upstream atomization, electric-field, capillary, viscous, and inertial groups are mainly used to correlate jet diameter, droplet diameter, and droplet-size reduction. For example, Wang et al. [159] correlated droplet-size reduction with Ca_e (The electric capillary number, represents the ratio of electric forcing to interfacial or surface-tension forces. $Ca_e = \frac{\varepsilon_0 V^2}{\gamma D h^2}$) and We, while Estrada-D et al. [156] used Buckingham-π-based groups to predict Taylor cone-jet diameter. These correlations define the spray state supplied to the heated surface, including droplet size, jet breakup behavior, spray dispersion, and liquid flux.

When the predicted quantity changes from droplet or jet characteristics to thermal response, the role of the dimensionless groups also changes. Tian et al. [35] linked atomization and heat transfer by correlating both D_{32} / D_0 and Nu, indicating that upstream droplet refinement and liquid supply provide the boundary conditions for downstream heat-transfer enhancement. Xu et al. [85] and Kim et al. [157] further showed that regime-dependent correlations are required when evaporation and boiling become important: the introduction of Ja reflects latent heat absorption, whereas the increasing role of Bo_E, We, N, and L^* / D_i indicates that electric forcing, liquid inertia, spray coverage, and geometric confinement modify the coupling between atomization and heat transfer. Therefore, the internal connection among these correlations lies in the transfer of dominant mechanisms from EHD atomization to droplet impact, liquid-film renewal, evaporation, boiling, and heat-transfer limits. Future correlations should therefore be developed as regime-aware models rather than universal formulas spanning unrelated operating regimes.

Although the above dimensionless correlations provide useful predictive tools for ESC, most remain semi-empirical and regime-specific. Their validity is usually constrained by the tested working fluid, nozzle geometry, applied voltage, flow rate, surface structure, and heat-transfer regime; therefore, direct extrapolation to new fluids, high-flow conditions, confined multi-nozzle chambers, or structured surfaces may introduce large uncertainty. Purely data-driven models offer an alternative, but they usually require large datasets and may lose physical consistency outside the training range.

Physics-informed machine learning (PIML) provides a potential framework for improving ESC prediction by embedding governing equations, conservation laws, boundary conditions, scaling relations, and dimensionless groups into data-driven learning [160]. PIML has been widely developed for nonlinear PDE-governed systems and fluid-mechanics problems, including flow-field reconstruction from limited measurements and physics-constrained prediction of velocity, pressure, and thermal fields in complex geometries [161–163]. In heat-transfer applications, physics-informed and hybrid machine-learning frameworks have also been explored for CHF prediction and convective heat-transfer coefficient estimation, demonstrating improved data efficiency, interpretability, and generalization compared with purely data-driven models [164,165]. For ESC, PIML could incorporate EHD atomization laws, charged-droplet transport, wall energy balance, evaporation and boiling constraints, and dimensionless parameters such as Bo_E, We, Re, Pr, Ja, and Nu. By using measurements of spray morphology, droplet diameter, wall temperature, heat flux, and voltage-current response, such models may link upstream atomization with downstream heat-transfer performance and support the prediction of spray-mode transition, HTC, CHF, and optimal operating windows under limited experimental data.

6.2 Numerical simulation and multiscale modeling of electrospray cooling

Numerical simulation has become an important tool for analyzing ESC because EHD atomization, charged droplet transport, wall-film renewal, evaporation, boiling, and dry-out occur across multiple length and time scales. In conventional spray cooling, VOF, level-set, Eulerian–Lagrangian, DPM, wall-film, and subgrid breakup models have been widely used to describe droplet impact, thin-film evolution, splashing, evaporation, and surface heat transfer [54,166–169]. For ESC, however, these processes are further coupled with electric-field force, interfacial charge transport, Coulombic interaction, induced airflow, and electrohydrodynamic modification of near-wall behavior. Therefore, ESC modeling requires a multiscale framework that couples EHD atomization, charged droplet transport, wall-film evolution, and surface heat transfer.

In the near-nozzle region, numerical simulation mainly aims to resolve meniscus deformation, Taylor cone formation, cone-to-jet transition, jet thinning, and primary breakup of the charged liquid jet. Interface-resolved methods, such as VOF, level-set, phase-field, and front-tracking methods, are suitable for this upstream EHD atomization process. López-Herrera et al. established a charge-conservative VOF framework for EHD two-phase flows [170]. Rahmanpour et al. then applied a VOF-based Taylor–Melcher model to simulate stable Taylor cone-jet formation [171], while Huh and Wirz extended OpenFOAM-based FVM/VOF modeling to predict jet breakup, emitted droplet size, spray current, and specific charge [172]. Further simulations resolved the velocity field, electric field, surface charge, energy dissipation, mode transition, and three-dimensional jet instability in the cone-to-jet region [173–175]. These studies provide key near-field source information for ESC, including droplet size, charge level, jet stability, and spray morphology. However, their high grid-resolution requirement makes them more suitable for near-field atomization analysis than for full device-scale heat-transfer prediction.

After primary breakup, the modeling focus shifts to charged droplet transport, evaporation, and deposition. In conventional spray cooling, Eulerian–Lagrangian and DPM approaches are commonly used to predict droplet trajectories, residence time, impingement flux, and droplet–gas momentum exchange [69,169]. For ESC, these models must additionally include electric-field acceleration, Coulombic repulsion, image-charge effects, and gas motion induced by charged droplet transport.

Arumugham-Achari et al. developed a two-way coupled Eulerian–Lagrangian framework that links three-dimensional Lagrangian droplet tracking with a two-dimensional Eulerian model for induced gas flow [176]. Arumugham-Achari et al. later incorporated evaporation, Coulomb explosions, vapor transport, gas-phase heat transfer, and residual-charge transport into evaporating electrospray simulations [177]. Brentjes et al. further modeled evaporating charged sprays by coupling Lagrangian droplet tracking with electrostatic-field calculation, gas-phase heat and vapor transport, and residual-charge transport [178]. Jiang et al. also showed that voltage and nozzle-to-collector distance regulate droplet spreading, deposition diameter, spray angle, and droplet spacing through the balance between electric-field force and Coulombic repulsion [179]. These works indicate that Eulerian–Lagrangian models are essential for translating near-nozzle atomization outputs into pre-impact droplet size, velocity, charge level, mass flux, and spatial deposition pattern for ESC heat-transfer prediction.

Further prediction of ESC performance requires coupling droplet transport with wall-film dynamics and heat transfer. Although wall-side models for droplet impact, spreading, splashing, film formation, evaporation, and boiling have been substantially developed in conventional spray cooling, ESC involves additional near-wall electric effects, including droplet charge retention and transfer, image-charge attraction, dielectrophoretic force, electrowetting-induced contact-line motion, surface charge accumulation, electric-field-induced bubble deformation, and electrostatic stresses at liquid–vapor interfaces. These factors may modify droplet deposition, liquid-film thickness, contact angle, bubble departure, vapor removal, dry-out, and rewetting behavior. Wan et al. coupled DPM with a Lagrangian wall-film model to describe charged droplet transport, evaporation, droplet impact, film formation, and wall-film heat transfer in ESC [115]. They later developed a VOF–DPM–LWF framework, in which VOF resolved Taylor cone formation and cone-jet evolution, DPM described charged droplet dispersion, and LWF captured droplet impact and wall-film heat transfer [180]. This coupling provides a useful route for connecting near-nozzle EHD atomization with downstream droplet transport and wall-side heat-transfer prediction, but a dedicated wall-side model for charged droplet impact, EHD-modified liquid-film dynamics, boiling, and conjugate heat transfer has not yet been well established.

Microscale and mesoscale simulations can complement continuum-scale models by revealing mechanisms that are difficult to resolve using VOF, DPM, or LWF methods. Molecular dynamics simulations have been used to explain how surfactants and nanoparticles modify intermolecular interactions, molecular clustering, charge distribution, Taylor cone formation, jet length, and cluster generation in cone-jet electrospray [114,118]. At the wall side, pseudopotential LBM simulations of channel flow boiling showed that electric stress can elongate bubbles, reduce bubble departure size, promote bubble detachment, and weaken bubble–bubble coalescence under multi-nucleation conditions [147]. Although these studies are not complete ESC heat-transfer models, they provide useful microscopic and mesoscopic insight into working-fluid effects, vapor removal, rewetting, and CHF-related behavior.

7 Conclusions and Outlook

7.1 Conclusions

This review summarizes the fundamental mechanisms, spray-mode evolution, heat-transfer enhancement strategies, and predictive approaches of electrospray cooling (ESC) for high-heat-flux thermal management. Unlike conventional spray cooling, ESC is governed by the coupling between electrohydrodynamic atomization and phase-change heat transfer. The applied electric field modifies the interfacial force balance at the nozzle, where Maxwell electric stress competes with capillary pressure, viscous resistance, liquid inertia, gravity, and liquid-supply constraints. This force balance determines Taylor cone formation, jet breakup, charged-droplet generation, and spray-mode transition, which subsequently define the droplet-scale boundary conditions imposed on the heated surface.

A central conclusion of this review is that spray mode provides the physical bridge between upstream atomization and downstream heat-transfer performance. Stable continuous modes, especially cone-jet and well-controlled multi-jet or simple-jet regimes, generally produce smaller charged droplets, more uniform liquid-flux distribution, stronger surface coverage, and more effective liquid-film renewal. These features promote droplet–wall interaction, liquid spreading, evaporation, bubble departure, and surface rewetting. In contrast, periodic modes or unstable jetting may cause intermittent liquid delivery, non-uniform deposition, splashing, off-target liquid loss, thick-film accumulation, or local dry-out, thereby weakening the heat-transfer coefficient and reducing the available CHF margin.

The reviewed enhancement strategies indicate that ESC performance is controlled by the coordinated regulation of working-fluid properties, spray parameters, nozzle geometry, and surface morphology. Working-fluid modification affects electrical conductivity, charge relaxation, surface tension, volatility, latent heat, and atomization stability. Voltage and flow rate jointly determine the operating window of stable spray modes and the effective liquid supply to the heated wall. Nozzle and emitter designs regulate local electric-field distribution and spray uniformity, while surface modification influences wettability, nucleation-site density, capillary rewetting, bubble dynamics, and vapor-escape pathways. Therefore, heat-transfer enhancement in ESC should not be evaluated only by the instantaneous heat-transfer coefficient, but also by liquid replenishment, dry-out suppression, vapor removal, and CHF delay.

Existing dimensionless correlations, numerical simulations, and physics-informed prediction methods provide useful tools for ESC analysis, but they remain limited by regime dependence and incomplete multiphysics coupling. Current correlations are usually valid only within specific ranges of working fluid, nozzle configuration, voltage, flow rate, surface condition, and heat-transfer regime. Future predictive frameworks should therefore connect EHD atomization, charged-droplet transport, wall-film evolution, boiling heat transfer, and CHF prediction within a unified, regime-aware model.

7.2 Outlook

Based on these conclusions, future research on ESC should move from isolated performance optimization toward mechanism-resolved, reliable, and scalable cooling systems. The following directions are particularly important.

First, future work should develop environmentally compatible dielectric working fluids with balanced electrical and thermal properties. An ideal ESC coolant should simultaneously provide high dielectric strength, suitable electrical conductivity, low surface tension, low boiling point, high latent heat, material compatibility, and low environmental impact. Binary or ternary mixtures, surfactant-modified dielectric liquids, and low-GWP fluorinated fluids are promising candidates, but their effects on charge relaxation, cone-jet stability, droplet-size distribution, evaporation, boiling, and long-term chemical stability need to be evaluated systematically.

Second, stable high-throughput electrospray operation remains a key bottleneck for practical high-heat-flux cooling. Most stable cone-jet studies are conducted at relatively low flow rates, whereas practical electronic cooling requires larger liquid supply and spatially uniform coverage. Future studies should therefore establish operating maps for high-flow cone-jet, multi-jet, and stable simple-jet regimes by coupling applied voltage, flow rate, nozzle geometry, electrode spacing, and fluid properties. In particular, the upper stability limits associated with whipping instability, over-dispersion, splashing, corona discharge, and off-target liquid loss should be quantified.

Third, nozzle and array design should be optimized for both atomization stability and surface liquid-flux uniformity. Hemispherical emitters, porous extenders, MEMS-fabricated emitter arrays, and multiplexed electrospray devices provide possible routes for increasing total flow rate while maintaining fine droplet generation. However, array-scale interactions, electric-field shielding, jet-to-jet interference, non-uniform droplet deposition, and clogging resistance remain insufficiently understood. Future designs should therefore integrate electric-field regulation, hydraulic distribution, anti-clogging strategies, and compact packaging.

Fourth, surface engineering for ESC should shift from simple area enlargement to coupled liquid–vapor transport control. Structured surfaces should be designed to guide charged-droplet deposition, enhance wettability, sustain capillary rewetting, provide stable nucleation sites, and construct vapor-escape pathways. Ordered porous surfaces, hierarchical micro/nano-structures, and vapor–liquid separation architectures are especially promising for delaying dry-out and increasing CHF. Their interaction with local electric-field distortion, electrowetting, bubble deformation, and charged liquid-film dynamics requires further investigation.

Fifth, predictive modeling should be developed as a coupled, regime-aware framework. Existing correlations and simulations are mostly valid for limited fluids, geometries, and heat-transfer regimes. Future models should connect EHD atomization, charged-droplet transport, droplet impact, liquid-film evolution, evaporation, boiling, and CHF onset. Multiscale numerical simulations and physics-informed machine learning can be used to combine experimental data, conservation laws, electrostatic constraints, and dimensionless scaling, thereby improving prediction of spray-mode transition, HTC, CHF, and optimal operating windows under limited data.

Finally, long-term reliability and system integration must be addressed before ESC can be deployed in practical electronics cooling. Future studies should examine electrode corrosion, dielectric breakdown, charge accumulation, nozzle fouling, additive degradation, surface aging, coolant recovery, and closed-loop stability under continuous operation. In addition, compact high-voltage power supplies, feedback control of voltage and flow rate, liquid recirculation, electrical insulation, and compatibility with chip packaging should be integrated into module-level ESC demonstrations.

Table 5: Latin Symbols

Symbol	Description	Unit	Symbol	Description	Unit
A_{tot}	Total heat exchange area	m^2	k	Thermal conductivity of the fluid	$W/(m \cdot K)$
A_s	Increased surface area due to modification	m^2	k_{Cu}	Thermal conductivity of the copper block	$W/(m \cdot K)$
A_b	Substrate area	m^2	L	Characteristic length scale	m
A_r	Area ratio (A_{tot} / A_b)	-	M	Molar mass	kg/mol
c_p	Specific heat capacity at constant pressure	$J/(kg \cdot K)$	m	Mass flow rate	kg/s
D_i	Inner diameter of the nozzle/capillary	m	P	Parachor constant	-
D_o	Outer diameter of the nozzle/capillary	m	Q	Volumetric flow rate	m^3/s
d	Droplet diameter / Characteristic dimension	m	q	Surface heat flux	W/m^2
d_j	Jet diameter	m	q_e	Liquid charge density	C/m^3
D_{32}	Sauter mean diameter	m	q_{eff}	Effective heat flux	W/m^2
E	Electric field strength	V/m	q_{CHF}	Critical Heat Flux (CHF)	W/m^2
f	Area ratio (A_s / A_b)	-	T_{sat}	Saturation temperature	K or $^{\circ}C$
F_e	Electric body force density	N/m^3	T_s	Surface temperature	K or $^{\circ}C$
H	Nozzle-to-surface distance	m	T_a	Ambient temperature	K or $^{\circ}C$
h	Average heat transfer coefficient	$W/(m^2 \cdot K)$	T_l	Liquid inlet temperature	K or $^{\circ}C$
h_a	Air convective heat transfer coefficient	$W/(m^2 \cdot K)$	U	Fluid velocity	m/s
h_{fg}	Latent heat of vaporization	J/kg	V	Applied voltage	V
I	Electric current	A	w	Mass fraction (in mixture)	-
K	Electrical conductivity	S/m	x	Mole fraction (in mixture)	-

Table 6: Greek Symbols

Symbol	Description	Unit	Symbol	Description	Unit
α	Spray cone angle	°	ρ	Fluid density	kg/m^3
Δp	Pressure difference	Pa	σ	Surface	N/m
ΔT	Temperature difference	K	θ	Contact angle	°
ε_0	Vacuum permittivity ($\approx 8.854\times10^{-12}$)	F / m	ϕ	Electric potential	V
ε_l	Liquid permittivity	F / m	ϕ_i	Volume fraction (in mixture)	-
μ	Dynamic viscosity	$Pa\cdot s$			

Table 7: Dimensionless Numbers

Symbol	Name	Physical Meaning
Bo_E	Electric Bond number	Ratio of electric forces to surface tension
Ja	Jakob number	Ratio of sensible heat to latent heat
Nu	Nusselt number	Ratio of convective heat transfer to conduction
Pr	Prandtl number	Ratio of momentum diffusivity to thermal diffusivity
Re	Reynolds number	Ratio of inertial forces to viscous foces
We	Weber number	Ratio of inertial forces to surface tension
Ca_e	Electric Capillary Number	the ratio between the electric force and the interfacial tension force

Table 8: Abbreviations

Acronym	Full Name
CHF	Critical Heat Flux
EHD	Electrohydrodynamics
ESC	Electrospray Cooling
SMD	Sauter Mean Diameter
HTC	Heat Transfer Coefficient
LFP	Leidenfrost Point
MES	Multiplexed Electrospray
MPCM	Microencapsulated Phase Change Material
RSM	Response Surface Methodology
SEM	Scanning Electron Microscope
STA	Surface with Thermal bridge and Air-extraction channel

Data availability

No data was used for the research described in the article.

References:

[1] E. Pop, Energy dissipation and transport in nanoscale devices, Nano Res. 3 (2010) 147–169. https://doi.org/10.1007/s12274-010-1019-z.

[2] Z. Wu, Z. Wang, Cooling next-generation electronics: From emerging semiconductors to data centers, Innov. Energy 2 (2025) 100125–3. https://doi.org/10.59717/j.xinn-energy.2025.100125.

[3] T. Dbouk, O. Mourad, A Review on Thermal Management and Heat Dissipation Strategies for 5G and 6G Base Stations: Challenges and Solutions, Energies 18 (2025) 1355. https://doi.org/10.3390/en18061355.

[4] L. He, Z. Gu, Y. Zhang, H. Jing, P. Li, Review on thermal management of lithium-ion batteries for electric vehicles: advances, challenges, and outlook, Energy Fuels 37 (2023) 4835–4857. https://doi.org/10.1021/acs.energyfuels.2c04243.

[5] F.S. Hwang, T. Confrey, C. Reidy, D. Picovici, D. Callaghan, D. Culliton, C. Nolan, Review of battery thermal management systems in electric vehicles, Renew. Sustain. Energy Rev. 192 (2024) 114171. https://doi.org/10.1016/j.rser.2023.114171.

[6] L. Zhou, S. Zhang, A. Jain, X. Li, Recent advances in indirect liquid cooling of lithium-ion batteries, J. Energy Storage 132 (2025) 117750. https://doi.org/10.1016/j.est.2025.117750.

[7] Y. Song, M. Yang, Z. Zheng, F. Cao, Y. Ma, W. Wang, X. Wang, T. Yang, X. Pang, G. Bai, X. Wang, M. Sun, Future development trends in new energy vehicle thermal management technology in the context of carbon neutrality and global hydrofluorocarbon regulations, Innov. Energy 2 (2025) 100116–22. https://doi.org/10.59717/j.xinn-energy.2025.100116.

[8] A. Behzadi-Moghaddam, Z. Ghasemi, J. Hashemi, M. Pasandideh-Fard, M. Sardarabadi, Evaluation of jet impingement cooling for high heat-flux chips using taguchi method and machine learning approach: An experimental study, Int. J. Therm. Sci. 220 (2026) 110387. https://doi.org/10.1016/j.ijthermalsci.2025.110387.

[9] J.R. Black, Electromigration—A brief survey and some recent results, IEEE Trans. Electron Devices 16 (1969) 338–347. https://doi.org/10.1109/T-ED.1969.16754.

[10] I. Mudawar, Assessment of high-heat-flux thermal management schemes, IEEE Trans. Compon. Packag. Technol. 24 (2001) 122–141. https://doi.org/10.1109/6144.926375.

[11] V. Nair, A. Baby, A. M.B., I. S., M. Murali, M.B. Nair, A comprehensive review of air-cooled heat sinks for thermal management of electronic devices, Int. Commun. Heat Mass Transf. 159 (2024) 108055. https://doi.org/10.1016/j.icheatmasstransfer.2024.108055.

[12] J.J. Huddle, L.C. Chow, S. Lei, A. Marcos, D.P. Rini, S.J. Lindauer,

M. Bass, P.J. Delfyett, Thermal management of diode laser arrays, in: Sixt. Annu. IEEE Semicond. Therm. Meas. Manag. Symp. Cat No00CH37068, 2000: pp. 154–160. https://doi.org/10.1109/STHERM.2000.837078.

[13] X. Wang, Q. Wen, J. Yang, J. Xiang, Z. Wang, C. Weng, F. Chen, S. Zheng, A review on data centre cooling system using heat pipe technology, Sustain. Comput. Inform. Syst. 35 (2022) 100774. https://doi.org/10.1016/j.suscom.2022.100774.

[14] N. Uddin, P.T.W. Kee, B. Weigand, Heat transfer by jet impingement: A review of heat transfer correlations and high-fidelity simulations, Appl. Therm. Eng. 257 (2024) 124258. https://doi.org/10.1016/j.applthermaleng.2024.124258.

[15] M.G. Khan, A. Fartaj, A review on microchannel heat exchangers and potential applications, Int. J. Energy Res. 35 (2011) 553–582. https://doi.org/10.1002/er.1720.

[16] F. Zhou, W. Gu, G. Ma, Microchannel heat sinks for cold plate liquid cooling in data centers: Advances, evaluations and prospects, Renew. Sustain. Energy Rev. 230 (2026) 116729. https://doi.org/10.1016/j.rser.2026.116729.

[17] R. Kong, H. Zhang, M. Tang, H. Zou, C. Tian, T. Ding, Enhancing data center cooling efficiency and ability: A comprehensive review of direct liquid cooling technologies, Energy 308 (2024) 132846. https://doi.org/10.1016/j.energy.2024.132846.

[18] H.N. Chaudhry, B.R. Hughes, S.A. Ghani, A review of heat pipe systems for heat recovery and renewable energy applications, Renew. Sustain. Energy Rev. 16 (2012) 2249–2259. https://doi.org/10.1016/j.rser.2012.01.038.

[19] S. Zhong, R. Xie, Y. Li, X. Sun, Operational Characteristics of Loop Heat Pipe in Microgravity and Normal Gravity Environments, J. Therm. Sci. 33 (2024) 1394–1408. https://doi.org/10.1007/s11630-024-1955-7.

[20] P.S. Yadav, R. Gautam, S. Bhan, H. Caliskan, A novel investigation on thermal performance and start-up of pulsating heat pipe at microgravity, J. Therm. Anal. Calorim. 150 (2025) 14615–14632. https://doi.org/10.1007/s10973-025-14539-4.

[21] D.B. Tuckerman, R.F.W. Pease, High-performance heat sinking for VLSI, IEEE Electron Device Lett. 2 (1981) 126–129. https://doi.org/10.1109/EDL.1981.25367.

[22] Y. Miao, T. Zhang, X. Xu, S. Yang, H. Chen, H. Huang, A comprehensive review on advanced microchannel cooling technologies: two-phase thermal management and machine learning applications, Appl. Therm. Eng. 279 (2025) 127697. https://doi.org/10.1016/j.applthermaleng.2025.127697.

[23] H. Martin, Heat and Mass Transfer between Impinging Gas Jets and Solid Surfaces, in: Adv. Heat Transf., Elsevier, 1977: pp. 1–60. https://doi.org/10.1016/S0065-2717(08)70221-1.

[24] W. Deng, A. Gomez, Electrospray cooling for microelectronics, Int. J. Heat Mass Transf. 54 (2011) 2270–2275.

https://doi.org/10.1016/j.ijheatmasstransfer.2011.02.038.

[25] A. Jaworek, A.T. Sobczyk, Electrospraying route to nanotechnology: An overview, J. Electrost. 66 (2008) 197–219. https://doi.org/10.1016/j.elstat.2007.10.001.

[26] J.Y. Kim, S.J. Lee, J.G. Hong, Spray mode and monodisperse droplet properties of an electrospray, ACS Omega 7 (2022) 28667–28674. https://doi.org/10.1021/acsomega.2c04002.

[27]Y. Shao, J. Wang, H. Wang, X. Zhou, Z. Xie, X. Zhu, Y. Ding, R. Chen, Q. Liao, Characterization of dynamics and heat transfer in electro-spray at elevated flow rates, Int. J. Heat Mass Transf. 226 (2024) 125473. https://doi.org/10.1016/j.ijheatmasstransfer.2024.125473.

[28] R. Xu, G. Wang, P. Jiang, Spray Cooling on Enhanced Surfaces: A Review of the Progress and Mechanisms, J. Electron. Packag. 144 (2022) 010802. https://doi.org/10.1115/1.4050046.

[29] A. Faghri, Heat pipes: review, opportunities and challenges, in: Front. Heat Pipes, 2014. https://doi.org/10.5098/fhp.5.1.

[30] N. Gilmore, V. Timchenko, C. Menictas, Microchannel cooling of concentrator photovoltaics: A review, Renew. Sustain. Energy Rev. 90 (2018) 1041–1059. https://doi.org/10.1016/j.rser.2018.04.010.

[31] S. Sarkar, R. Gupta, T. Roy, R. Ganguly, C.M. Megaridis, Review of jet impingement cooling of electronic devices: Emerging role of surface engineering, Int. J. Heat Mass Transf. 206 (2023) 123888. https://doi.org/10.1016/j.ijheatmasstransfer.2023.123888.

[32] G.R.D. Prabhu, E.R. Williams, M. Wilm, P.L. Urban, Mass spectrometry using electrospray ionization, Nat. Rev. Methods Primer 3 (2023) 23. https://doi.org/10.1038/s43586-023-00203-4.

[33] S.N. Jayasinghe, Electrospray printing: Unravelling the history of a support free three-dimensional additive manufacturing technology, Mater. Today 62 (2023) 14–20. https://doi.org/10.1016/j.mattod.2022.12.006.

[34] P. Mallalieu, M. Jugroot, Multimodal electrospray thruster for small spacecraft: design and experimental characterization, J. Electr. Propuls. 3 (2024) 12. https://doi.org/10.1007/s44205-024-00075-0.

[35] J. Tian, L. Kong, B. Li, Y. Chen, Z. Wang, J. Wang, B. Chen, J. Xiong, Experimental investigation on heat transfer performance during electrospray cooling with ethanol–R141b mixture, Appl. Therm. Eng. 230 (2023) 120879. https://doi.org/10.1016/j.applthermaleng.2023.120879.

[36] M.A. Shah, Y. Kim, S.T.H. Zaidi, Y. Lee, D.-G. Lee, S. Hur, Design and simulation of a hybrid inkjet printhead for ejecting high viscous inks, Microsyst. Technol. 31 (2025) 1411–1421. https://doi.org/10.1007/s00542-024-05785-x.

[37] S. Appah, P. Wang, M. Ou, C. Gong, W. Jia, Review of electrostatic system parameters, charged droplets characteristics and substrate impact

behavior from pesticides spraying, Int. J. Agric. Biol. Eng. 12 (2019) 1–9. https://doi.org/10.25165/j.ijabe.20191202.4673.

[38] A. Jaworek, A.T. Sobczyk, A. Krupa, Electrospray application to powder production and surface coating, J. Aerosol Sci. 125 (2018) 57–92. https://doi.org/10.1016/j.jaerosci.2018.04.006.

[39] C. Wang, Y. Zhou, Electrospray of core–shell micro drug carriers with various experimental and material parameters, Int. J. Adv. Manuf. Technol. 137 (2025) 843–855. https://doi.org/10.1007/s00170-025-15279-3.

[40] G. Liang, I. Mudawar, Review of spray cooling – Part 1: Single-phase and nucleate boiling regimes, and critical heat flux, Int. J. Heat Mass Transf. 115 (2017) 1174–1205. https://doi.org/10.1016/j.ijheatmasstransfer.2017.06.029.

[41] G. Liang, I. Mudawar, Review of spray cooling – Part 2: High temperature boiling regimes and quenching applications, Int. J. Heat Mass Transf. 115 (2017) 1206–1222. https://doi.org/10.1016/j.ijheatmasstransfer.2017.06.022.

[42] P. GaneshKumar, V. Sivalingam, V.S. Vigneswaran, V. Ramalingam, K. Seong Cheol, R. Vanaraj, Spray cooling for hydrogen vehicle, electronic devices, solar and building (low temperature) applications: A state-of-art review, Renew. Sustain. Energy Rev. 189 (2024) 113931. https://doi.org/10.1016/j.rser.2023.113931.

[43] H. Xu, J. Wang, Z. Wang, H. Wang, K. Yu, W. Zhang, L. Zuo, H.-B. Kim, Review of electrospray cooling and charged droplets heat transfer, Phys. Fluids 37 (2025). https://doi.org/10.1063/5.0299519.

[44] Z. Wang, Y. Chen, J. Xue, B. Li, J. Wang, Q. Dong, Electrospray modes of liquids in electrohydrodynamic atomization: A review, Phys. Fluids 36 (2024) 111304. https://doi.org/10.1063/5.0239267.

[45] J. Rosell-Llompart, J. Grifoll, I.G. Loscertales, Electrosprays in the cone-jet mode: From Taylor cone formation to spray development, J. Aerosol Sci. 125 (2018) 2–31. https://doi.org/10.1016/j.jaerosci.2018.04.008.

[46] A.M. Gañán-Calvo, J.M. López-Herrera, M.A. Herrada, A. Ramos, J.M. Montanero, Review on the physics of electrospray: From electrokinetics to the operating conditions of single and coaxial Taylor cone-jets, and AC electrospray, J. Aerosol Sci. 125 (2018) 32–56. https://doi.org/10.1016/j.jaerosci.2018.05.002.

[47] Z. Esa, M. Abid, J.H. Zaini, B. Aissa, M.M. Nauman, Advancements and applications of electrohydrodynamic printing in modern microelectronic devices: a comprehensive review, Appl. Phys. A 128 (2022) 780. https://doi.org/10.1007/s00339-022-05796-3.

[48] M.J. Gibbons, A.J. Robinson, Heat transfer characteristics of single cone-jet electrosprays, Int. J. Heat Mass Transf. 113 (2017) 70–83. https://doi.org/10.1016/j.ijheatmasstransfer.2017.04.119.

[49] R. Kandasamy, J.Y. Ho, P. Liu, T.N. Wong, K.C. Toh, S.J. Chua, Two-phase spray cooling for high ambient temperature data centers: Evaluation of

system performance, Appl. Energy 305 (2022) 117816. https://doi.org/10.1016/j.apenergy.2021.117816.

[50] X. Chen, S. Wu, Progress of aerospace-based spray cooling applications, Front. Energy Res. 10 (2022). https://doi.org/10.3389/fenrg.2022.968506.

[51] P. Fu, L. Zhao, X. Wang, J. Sun, Z. Xin, A Review of Cooling Technologies in Lithium-Ion Power Battery Thermal Management Systems for New Energy Vehicles, Processes 11 (2023) 3450. https://doi.org/10.3390/pr11123450.

[52] A. Jaworek, A. Krupa, Classification of the modes of EHD spraying, J. Aerosol Sci. 30 (1999) 873–893. https://doi.org/10.1016/S0021-8502(98)00787-3.

[53] A.G. Pautsch, T.A. Shedd, Spray impingement cooling with single- and multiple-nozzle arrays. Part I: Heat transfer data using FC-72, Int. J. Heat Mass Transf. 48 (2005) 3167–3175. https://doi.org/10.1016/j.ijheatmasstransfer.2005.02.012.

[54]R.P. Selvam, L. Lin, R. Ponnappan, Direct simulation of spray cooling: Effect of vapor bubble growth and liquid droplet impact on heat transfer, Int. J. Heat Mass Transf. 49 (2006) 4265–4278. https://doi.org/10.1016/j.ijheatmasstransfer.2006.05.009.

[55] M.R. Pais, L.C. Chow, E.T. Mahefkey, Surface roughness and its effects on the heat transfer mechanism in spray cooling, J. Heat Transf. 114 (1992) 211–219. https://doi.org/10.1115/1.2911248.

[56] W. Cheng, H. Chen, L. Hu, W. Zhang, Effect of droplet flash evaporation on vacuum flash evaporation cooling: Modeling, Int. J. Heat Mass Transf. 84 (2015) 149–157. https://doi.org/10.1016/j.ijheatmasstransfer.2014.12.078.

[57] D.P. Rini, R.-H. Chen, L.C. Chow, Bubble Behavior and Nucleate Boiling Heat Transfer in Saturated FC-72 Spray Cooling, J. Heat Transf. 124 (2002) 63–72. https://doi.org/10.1115/1.1418365.

[58] W.-L. Cheng, F.-Y. Han, Q.-N. Liu, R. Zhao, H. Fan, Experimental and theoretical investigation of surface temperature non-uniformity of spray cooling, Energy 36 (2011) 249–257. https://doi.org/10.1016/j.energy.2010.10.044.

[59] Y.B. Tan, J.L. Xie, F. Duan, T.N. Wong, K.C. Toh, K.F. Choo, P.K. Chan, Y.S. Chua, Multi-nozzle spray cooling for high heat flux applications in a closed loop system, Appl. Therm. Eng. 54 (2013) 372–379. https://doi.org/10.1016/j.applthermaleng.2013.01.033.

[60] I. Vladyko, N. Miskiv, K. Pavlenko, A. Chernyavskiy, A. Surtaev, Heat transfer peculiarities and crisis phenomena development in spray cooling using various types of nozzles, Int. Commun. Heat Mass Transf. 159 (2024) 108145. https://doi.org/10.1016/j.icheatmasstransfer.2024.108145.

[61] H. Chen, W. Cheng, Y. Peng, W. Zhang, L. Jiang, Experimental study on optimal spray parameters of piezoelectric atomizer based spray cooling, Int. J. Heat Mass Transf. 103 (2016) 57–65. https://doi.org/10.1016/j.ijheatmasstransfer.2016.07.037.

[62] R. Zeng, H. Kang, M. Umar, X. Liang, Y. Zhao, Design and thermal management study of fuel cell spray cooling system, Appl. Therm. Eng. 270 (2025) 126271. https://doi.org/10.1016/j.applthermaleng.2025.126271.

[63] W.-L. Cheng, Y.-H. Peng, H. Chen, L. Hu, H.-P. Hu, Experimental investigation on the heat transfer characteristics of vacuum spray flash evaporation cooling, Int. J. Heat Mass Transf. 102 (2016) 233–240. https://doi.org/10.1016/j.ijheatmasstransfer.2016.05.140.

[64] J.L. Xie, Z.W. Gan, T.N. Wong, F. Duan, S.C.M. Yu, Y.H. Wu, Thermal effects on a pressure swirl nozzle in spray cooling, Int. J. Heat Mass Transf. 73 (2014) 130–140. https://doi.org/10.1016/j.ijheatmasstransfer.2014.01.077.

[65] F.M. Tenzer, I.V. Roisman, C. Tropea, Fast transient spray cooling of a hot thick target, J. Fluid Mech. 881 (2019) 84–103. https://doi.org/10.1017/jfm.2019.743.

[66] S.-S. Hsieh, Y.-F. Hsu, M.-L. Wang, A microspray-based cooling system for high powered LEDs, Energy Convers. Manag. 78 (2014) 338–346. https://doi.org/10.1016/j.enconman.2013.10.066.

[67] S.-S. Hsieh, S.-Y. Luo, Droplet impact dynamics and transient heat transfer of a micro spray system for power electronics devices, Int. J. Heat Mass Transf. 92 (2016) 190–205. https://doi.org/10.1016/j.ijheatmasstransfer.2015.08.099.

[68] W. He, Z. Luo, X. Deng, Z. Xia, A novel spray cooling device based on a dual synthetic jet actuator integrated with a piezoelectric atomizer, Heat Mass Transf. 56 (2020) 1551–1563. https://doi.org/10.1007/s00231-019-02804-w.

[69] J.-X. Li, Y.-Z. Li, E.-H. Li, T. Li, Numerical Investigation on the Thermodynamic Characteristics of a Liquid Film upon Spray Cooling Using an Air-Blast Atomization Nozzle, Entropy 22 (2020) 308. https://doi.org/10.3390/e22030308.

[70] J.-X. Li, Y.-Z. Li, B.-Y. Cai, E.-H. Li, Experimental Investigation on Heat Transfer Mechanism of Air-Blast-Spray-Cooling System with a Two-Phase Ejector Loop for Aeronautical Application, Energies 12 (2019) 3963. https://doi.org/10.3390/en12203963.

[71] M. Shafaee, M.H. Sabour, A. Abdehkakha, A. Elkaie, A visual study on the spray of gas-liquid atomizer, (2021). https://doi.org/10.48550/ARXIV.2106.04610.

[72] P.H.G. Allen, T.G. Karayiannis, Electrohydrodynamic enhancement of heat transfer and fluid flow, Heat Recovery Syst. CHP 15 (1995) 389–423.

https://doi.org/10.1016/0890-4332(95)90050-0.

[73] S. Ahangar Zonouzi, H. Aminfar, M. Mohammadpourfard, A review on effects of magnetic fields and electric fields on boiling heat transfer and CHF, Appl. Therm. Eng. 151 (2019) 11–25. https://doi.org/10.1016/j.applthermaleng.2019.01.099.

[74] R.P.A. Hartman, D.J. Brunner, D.M.A. Camelot, J.C.M. Marijnissen, B. Scarlett, Electrohydrodynamic atomization in the cone–jet mode physical modeling of the liquid cone and jet, J. Aerosol Sci. 30 (1999) 823–849. https://doi.org/10.1016/S0021-8502(99)00033-6.

[75] G. Taylor, Disintegration of Water Drops in an Electric Field, Proc. R. Soc. Lond. Ser. Math. Phys. Sci. 280 (1964) 383–397.

[76] J.F. de la Mora, The fluid dynamics of taylor cones, Annu. Rev. Fluid Mech. 39 (2007) 217–243. https://doi.org/10.1146/annurev.fluid.39.050905.110159.

[77] M. Cloupeau, B. Prunet-Foch, Electrostatic spraying of liquids: Main functioning modes, J. Electrost. 25 (1990) 165–184. https://doi.org/10.1016/0304-3886(90)90025-Q.

[78] H.-H. Kim, J.-H. Kim, A. Ogata, Time-resolved high-speed camera observation of electrospray, J. Aerosol Sci. 42 (2011) 249–263. https://doi.org/10.1016/j.jaerosci.2011.01.007.

[79] Z. Wang, R. Li, L. Tian, L. Xia, S. Zhan, J. Wang, J. Tu, Visualization of periodic emission of drops with micro-dripping mode in electrohydrodynamic (EHD) atomization, Exp. Therm. Fluid Sci. 105 (2019) 307–315. https://doi.org/10.1016/j.expthermflusci.2019.04.009.

[80] G. Riboux, Á.G. Marín, I.G. Loscertales, A. Barrero, Whipping instability characterization of an electrified visco-capillary jet, J. Fluid Mech. 671 (2011) 226–253. https://doi.org/10.1017/S0022112010005586.

[81]L.L.F. Agostinho, B. Bos, A. Kamau, S.P. Brouwer, E.C. Fuchs, J.C.M. Marijnissen, Simple-jet mode electrosprays with water. Description, characterization and application in a single effect evaporation chamber, J. Aerosol Sci. 125 (2018) 237–250. https://doi.org/10.1016/j.jaerosci.2018.04.010.

[82] R. Yakut, Response surface methodology-based multi-nozzle optimization for electrospray cooling, Appl. Therm. Eng. 236 (2024) 121914. https://doi.org/10.1016/j.applthermaleng.2023.121914.

[83] J. Zeleny, The electrical discharge from liquid points, and a hydrostatic method of measuring the electric intensity at their surfaces, Phys. Rev. 3 (1914) 69–91. https://doi.org/10.1103/PhysRev.3.69.

[84] Lord Rayleigh, XX. *On the equilibrium of liquid conducting masses charged with electricity*, Lond. Edinb. Dublin Philos. Mag. J. Sci. 14 (1882) 184–186. https://doi.org/10.1080/14786448208628425.

[85] H. Xu, J. Wang, B. Li, K. Yu, H. Wang, J. Tian, B. Li, Electrospray characteristics and cooling performance of dielectric fluid HFE-7100, Energy

259 (2022) 125072. https://doi.org/10.1016/j.energy.2022.125072.

[86] H. Xu, J. Wang, Z. Wang, K. Yu, H. Xu, D. Wang, W. Zhang, Impact dynamics of a charged droplet onto different substrates, Phys. Fluids 33 (2021) 102111. https://doi.org/10.1063/5.0066381.

[87] H. Wan, P.J. Liu, F. Qin, X.G. Wei, W.Q. Li, Electrospray cooling characteristics in cone-jet and multi-jet modes, Int. J. Therm. Sci. 188 (2023) 108240. https://doi.org/10.1016/j.ijthermalsci.2023.108240.

[88] H. Xu, J. Wang, B. Li, K. Yu, J. Tian, D. Wang, W. Zhang, Effect of spray modes on electrospray cooling heat transfer of ethanol, Appl. Therm. Eng. 189 (2021) 116757. https://doi.org/10.1016/j.applthermaleng.2021.116757.

[89] E.D. Wilkes, S.D. Phillips, O.A. Basaran, Computational and experimental analysis of dynamics of drop formation, Phys. Fluids 11 (1999) 3577–3598. https://doi.org/10.1063/1.870224.

[90] X. Zhang, O.A. Basaran, Dynamics of drop formation from a capillary in the presence of an electric field, J. Fluid Mech. 326 (1996) 239–263. https://doi.org/10.1017/S0022112096008300.

[91] D.S. Hathi, P.M. Panchal, A. Sharma, R. Thaokar, A.M. Lakdawala, A numerical study on breakup of a liquid jet in an axial electric field, J. Aerosol Sci. 170 (2023) 106142. https://doi.org/10.1016/j.jaerosci.2023.106142.

[92] H. Xu, J. Wang, J. Tian, B. Li, J. Yao, L. Zuo, Y. Zhang, T. Zhao, Electrohydrodynamic disintegration of dielectric fluid blended with ethanol, Phys. Fluids 33 (2021) 062107. https://doi.org/10.1063/5.0052196.

[93] W. Yang, H. Duan, C. Li, W. Deng, Crossover of Varicose and Whipping Instabilities in Electrified Microjets, Phys. Rev. Lett. 112 (2014) 054501. https://doi.org/10.1103/PhysRevLett.112.054501.

[94] Z. Wang, Q. Dai, S. Yang, J. Tian, J. Wang, Y. Huo, J. Wang, An experimental study on the role of electrical conductivity in the steady cone-jet electrospray, Int. J. Multiph. Flow 171 (2024) 104696. https://doi.org/10.1016/j.ijmultiphaseflow.2023.104696.

[95] Z. Wang, Q. Kong, B. Li, J. Tian, K. Yu, J. Wang, Electrohydrodynamic instability and disintegration of low viscous liquid jet, Phys. Fluids 34 (2022) 123301. https://doi.org/10.1063/5.0130381.

[96] V. Taheri, H. Ebrahimi Rahnama, M.R. Morad, High flow rate electrospray cooling performance of water–ethanol mixtures, Appl. Therm. Eng. 239 (2024) 122200. https://doi.org/10.1016/j.applthermaleng.2023.122200.

[97] L.L.F. Agostinho, G. Tamminga, C.U. Yurteri, S.P. Brouwer, E.C. Fuchs, J.C.M. Marijnissen, Morphology of water electrosprays in the simple-jet mode, Phys. Rev. E 86 (2012) 066317. https://doi.org/10.1103/PhysRevE.86.066317.

[98] N. Abas, A.R. Kalair, N. Khan, A. Haider, Z. Saleem, M.S. Saleem, Natural and synthetic refrigerants, global warming: A review, Renew. Sustain. Energy Rev. 90 (2018) 557–569. https://doi.org/10.1016/j.rser.2018.03.099.

[99] R. Yakut, K. Yakut, E. Sabolsky, J. Kuhlman, Determination of heat transfer and spray performances of isopropyl alcohol electrospray, Sens. Actuators Phys. 332 (2021) 113135. https://doi.org/10.1016/j.sna.2021.113135.

[100] F. Sonmez, Experimental Study and Comparative Analysis of Electrospray Cooling Performance of Water Mixtures with Ethanol, Methanol, and Isopropyl Alcohol, Heat Transf. Res. (2025). https://doi.org/10.1615/HeatTransRes.2025061208.

[101] W. Evans, R. Prasher, J. Fish, P. Meakin, P. Phelan, P. Keblinski, Effect of aggregation and interfacial thermal resistance on thermal conductivity of nanocomposites and colloidal nanofluids, Int. J. Heat Mass Transf. 51 (2008) 1431–1438. https://doi.org/10.1016/j.ijheatmasstransfer.2007.10.017.

[102] P. Keblinski, S.R. Phillpot, S.U.S. Choi, J.A. Eastman, Mechanisms of heat flow in suspensions of nano-sized particles (nanofluids), Int. J. Heat Mass Transf. 45 (2002) 855–863. https://doi.org/10.1016/S0017-9310(01)00175-2.

[103] W. Yu, S.U.S. Choi, The role of interfacial layers in the enhanced thermal conductivity of nanofluids: a renovated maxwell model, J. Nanoparticle Res. 5 (2003) 167–171. https://doi.org/10.1023/A:1024438603801.

[104] C.-J. Yu, A.G. Richter, A. Datta, M.K. Durbin, P. Dutta, Molecular layering in a liquid on a solid substrate: an X-ray reflectivity study, Phys. B Condens. Matter 283 (2000) 27–31. https://doi.org/10.1016/S0921-4526(99)01885-2.

[105] J.W. Gao, R.T. Zheng, H. Ohtani, D.S. Zhu, G. Chen, Experimental Investigation of Heat Conduction Mechanisms in Nanofluids. Clue on Clustering, Nano Lett. 9 (2009) 4128–4132. https://doi.org/10.1021/nl902358m.

[106] W. Evans, J. Fish, P. Keblinski, Role of brownian motion hydrodynamics on nanofluid thermal conductivity, Appl. Phys. Lett. 88 (2006) 093116. https://doi.org/10.1063/1.2179118.

[107] E. Castillo-Orozco, A. Kar, R. Kumar, Electrospray mode transition of microdroplets with semiconductor nanoparticle suspension, Sci. Rep. 7 (2017) 5144. https://doi.org/10.1038/s41598-017-05175-6.

[108] R.C. Reid, J.M. Prausnitz, B.E. Poling, The properties of gases and liquids, 4th ed., McGraw-Hill, New York, 1989.

[109] N. Shardt, Y. Wang, Z. Jin, J.A.W. Elliott, Surface tension as a function of temperature and composition for a broad range of mixtures, Chem. Eng. Sci. 230 (2021) 116095. https://doi.org/10.1016/j.ces.2020.116095.

[110] W.J. Lyman, W.F. Reehl, D.H. Rosenblatt, Handbook of chemical property estimation methods: environmental behavior of organic compounds, McGraw-Hill, New York, 1982.

[111] J.C. Maxwell, A Treatise On Electricity And Magnetism, Oxford University Press, Oxford, 1998.

https://doi.org/10.1093/oso/9780198503743.001.0001.

[112] J. Wang, J.K. Carson, M.F. North, D.J. Cleland, A new approach to modelling the effective thermal conductivity of heterogeneous materials, Int. J. Heat Mass Transf. 49 (2006) 3075–3083. https://doi.org/10.1016/j.ijheatmasstransfer.2006.02.007.

[113] J.M. Smith, H.C. Van Ness, M.M. Abbott, Introduction to chemical engineering thermodynamics, 7th ed., McGraw-Hill, Boston, Mass., 2005.

[114] Q. Dai, Z. Wang, Y. Chen, B. Li, J. Wang, Q. Dong, J. Wang, Microscopic mechanism of nanofluids electrospray: A molecular dynamics study, Phys. Fluids 36 (2024) 072016. https://doi.org/10.1063/5.0220214.

[115] H. Wan, P.J. Liu, F. Qin, G.Q. He, W.Q. Li, Heat transfer enhancement of electrospray cooling with microencapsulated phase change material slurry (MPCMS): A comprehensive numerical model and experimental study, Int. J. Heat Mass Transf. 224 (2024) 125293. https://doi.org/10.1016/j.ijheatmasstransfer.2024.125293.

[116] Y.T. Aksoy, F. Enayati, P. Eneren, M.R. Vetrano, Experimental study on enhanced heat transfer via nanoparticle depositions using TiO2-water nanofluid sprays, Appl. Therm. Eng. 264 (2025) 125450. https://doi.org/10.1016/j.applthermaleng.2025.125450.

[117] F. Riaz Siddiqui, C.-Y. Tso, H. Qiu, C.Y.H. Chao, S. Chung Fu, Hybrid nanofluid spray cooling performance and its residue surface effects: Toward thermal management of high heat flux devices, Appl. Therm. Eng. 211 (2022) 118454. https://doi.org/10.1016/j.applthermaleng.2022.118454.

[118] Y. Li, Z. Wang, B. Li, J. Tian, K. Yu, Molecular dynamics simulation of the cone-jet electrospray: Role of surfactants, Int. J. Heat Mass Transf. 214 (2023) 124388. https://doi.org/10.1016/j.ijheatmasstransfer.2023.124388.

[119] A. Ranjan, R. Kumar, P.K. Panigrahi, A high performance aqueous surfactant solution for enhanced electrospray cooling, Int. J. Heat Mass Transf. 251 (2025) 127410. https://doi.org/10.1016/j.ijheatmasstransfer.2025.127410.

[120] Y.M. Qiao, S. Chandra, Experiments on Adding a Surfactant to Water Drops Boiling on a Hot Surface, Proc. Math. Phys. Eng. Sci. 453 (1997) 673–689.

[121] W.-W. Zhang, Y.-Y. Li, W.-J. Long, W.-L. Cheng, Enhancement mechanism of high alcohol surfactant on spray cooling: Experimental study, Int. J. Heat Mass Transf. 126 (2018) 363–376. https://doi.org/10.1016/j.ijheatmasstransfer.2018.05.130.

[122] P. Liu, R. Kandasamy, J.Y. Ho, H. Feng, T.N. Wong, Comparative study on the enhancement of spray cooling heat transfer using conventional and bio-surfactants, Appl. Therm. Eng. 194 (2021) 117047.

https://doi.org/10.1016/j.applthermaleng.2021.117047.

[123] B. Wang, Z. Liu, B. Zhang, Y. Xia, Z. Wang, G. Wang, Effect of Nanoparticle Type and Surfactant on Heat Transfer Enhancement in Spray Cooling, J. Therm. Sci. 29 (2020) 708–717. https://doi.org/10.1007/s11630-020-1212-7.

[124] S. Jowkar, M. Jafari, M.R. Morad, Heat transfer characteristics of high flow rate electrospray and droplet cooling, Appl. Therm. Eng. 162 (2019) 114239. https://doi.org/10.1016/j.applthermaleng.2019.114239.

[125] M.R. Morad, A. Rajabi, M. Razavi, S.R.P. Sereshkeh, A Very Stable High Throughput Taylor Cone-jet in Electrohydrodynamics, Sci. Rep. 6 (2016) 38509. https://doi.org/10.1038/srep38509.

[126] R. Yakut, K. Yakut, E. Sabolsky, J. Kuhlman, Experimental determination of cooling and spray characteristics of the water electrospray, Int. Commun. Heat Mass Transf. 120 (2021) 105046. https://doi.org/10.1016/j.icheatmasstransfer.2020.105046.

[127] L. Boston, P. Huang, P.R. Chiarot, Effect of nozzle orientation on electrospray cooling, Appl. Therm. Eng. 210 (2022) 118360. https://doi.org/10.1016/j.applthermaleng.2022.118360.

[128] H. Ebrahimi Rahnama, V. Taheri, F. Ebrahimi, M.R. Morad, The influence of a hemispherical porous extender on electrospray stability and cooling performance, Phys. Fluids 37 (2025) 083406. https://doi.org/10.1063/5.0281050.

[129] E.A. Silk, J. Kim, K. Kiger, Spray cooling of enhanced surfaces: Impact of structured surface geometry and spray axis inclination, Int. J. Heat Mass Transf. 49 (2006) 4910–4920. https://doi.org/10.1016/j.ijheatmasstransfer.2006.05.031.

[130] C.-C. Hsieh, S.-C. Yao, Evaporative heat transfer characteristics of a water spray on micro-structured silicon surfaces, Int. J. Heat Mass Transf. 49 (2006) 962–974. https://doi.org/10.1016/j.ijheatmasstransfer.2005.09.013.

[131] A.S. Salman, N.M. Abdulrazzaq, A. Tikadar, S.K. Oudah, J.A. Khan, Parametric study of heat transfer characteristics of enhanced surfaces in a spray cooling system: An experimental investigation, Appl. Therm. Eng. 183 (2021) 115824. https://doi.org/10.1016/j.applthermaleng.2020.115824.

[132] H. Bostanci, S.S. Altalidi, S. Nasrazadani, Two-phase spray cooling with HFC-134a and HFO-1234yf on practical enhanced surfaces, Appl. Therm. Eng. 131 (2018) 150–158. https://doi.org/10.1016/j.applthermaleng.2017.11.142.

[133] J.H. Kim, S.M. You, S.U.S. Choi, Evaporative spray cooling of plain and microporous coated surfaces, Int. J. Heat Mass Transf. 47 (2004) 3307–3315. https://doi.org/10.1016/j.ijheatmasstransfer.2004.01.018.

[134] S.J. Thiagarajan, S. Narumanchi, R. Yang, Effect of flow rate and subcooling on spray heat transfer on microporous copper surfaces, Int. J. Heat

Mass Transf. 69 (2014) 493–505. https://doi.org/10.1016/j.ijheatmasstransfer.2013.09.033.

[135] B. Horacek, K.T. Kiger, J. Kim, Single nozzle spray cooling heat transfer mechanisms, Int. J. Heat Mass Transf. 48 (2005) 1425–1438. https://doi.org/10.1016/j.ijheatmasstransfer.2004.10.026.

[136] C. Sodtke, P. Stephan, Spray cooling on micro structured surfaces, Int. J. Heat Mass Transf. 50 (2007) 4089–4097. https://doi.org/10.1016/j.ijheatmasstransfer.2006.12.037.

[137] Y. Hu, Y. Lei, X. Liu, R. Yang, Heat transfer enhancement of spray cooling by copper micromesh surface, Mater. Today Phys. 28 (2022) 100857. https://doi.org/10.1016/j.mtphys.2022.100857.

[138] M. Jiang, Y. Wang, F. Liu, H. Du, Y. Li, H. Zhang, S. To, S. Wang, C. Pan, J. Yu, D. Quéré, Z. Wang, Inhibiting the Leidenfrost effect above 1,000 °C for sustained thermal cooling, Nature 601 (2022) 568–572. https://doi.org/10.1038/s41586-021-04307-3.

[139] Q. Ni, W. Lu, X. Ling, Experimental and computational investigation on synergistic enhancement spray cooling using micropillars and capillary-driven wicking hybrid structures, Int. J. Heat Mass Transf. 217 (2023) 124643. https://doi.org/10.1016/j.ijheatmasstransfer.2023.124643.

[140] Y. Hu, Y. Lei, X. Liu, R. Yang, Record-high heat transfer performance of spray cooling on 3D-printed hierarchical micro/nano-structured surface, Sci. Bull. 70 (2025) 223–231. https://doi.org/10.1016/j.scib.2024.10.028.

[141] Z. Zhang, J. Li, P.-X. Jiang, Experimental investigation of spray cooling on flat and enhanced surfaces, Appl. Therm. Eng. 51 (2013) 102–111. https://doi.org/10.1016/j.applthermaleng.2012.08.057.

[142] A. Kabakuş, K. Yakut, A.N. Özakın, R. Yakut, Experimental determination of cooling performance on heat sinks with cone-jet electrospray mode, Eng. Sci. Technol. Int. J. 24 (2021) 665–670. https://doi.org/10.1016/j.jestch.2020.11.004.

[143] R. Yakut, Determining the cooling performance of the optimized nozzle electrospray cooling system with uniquely designed lattice heat sink, Int. J. Therm. Sci. 215 (2025) 109972. https://doi.org/10.1016/j.ijthermalsci.2025.109972.

[144] A. Kabakuş, K. Yakut, Optimization of finned heat sinks with electrospray cooling: full factorial method, Heat Transf. Res. 55 (2024). https://doi.org/10.1615/HeatTransRes.2023049860.

[145] J. Tian, C. He, Y. Chen, Z. Wang, Z. Zuo, J. Wang, B. Chen, J. Xiong, Experimental study on combined heat transfer enhancement due to macro-structured surface and electric field during electrospray cooling, Int. J. Heat Mass Transf. 220 (2024) 125015. https://doi.org/10.1016/j.ijheatmasstransfer.2023.125015.

[146] C. He, J. Tian, Y. Chen, Y. Zhu, X. Liu, H. Wang, Z. Wang, B.

Cai, C. Wang, J. Wang, Z. Zhou, B. Chen, Enhancing thin film boiling heat transfer through electric field and surface Macro-Structure Synergy: Insights from bubble dynamics modulation, Int. J. Heat Mass Transf. 249 (2025) 127264. https://doi.org/10.1016/j.ijheatmasstransfer.2025.127264.

[147] J.-D. Yao, K. Luo, J. Wu, H.-L. Yi, H.-P. Tan, Effect of electric field on bubble dynamics in channel flow boiling using lattice Boltzmann method, Int. J. Heat Fluid Flow 109 (2024) 109550. https://doi.org/10.1016/j.ijheatfluidflow.2024.109550.

[148] B. Liu, A.I. Garivalis, Z. Cao, Y. Zhang, J. Wei, P.D. Marco, Effects of electric field on pool boiling heat transfer over microstructured surfaces under different liquid subcoolings, Int. J. Heat Mass Transf. 183 (2022) 122154. https://doi.org/10.1016/j.ijheatmasstransfer.2021.122154.

[149] H. Chang, B. Liu, Q. Li, X. Yang, P. Zhou, Effects of electric field on pool boiling heat transfer over composite microstructured surfaces with microcavities on micro-pin-fins, Int. J. Heat Mass Transf. 205 (2023) 123893. https://doi.org/10.1016/j.ijheatmasstransfer.2023.123893.

[150] X. Quan, M. Gao, P. Cheng, J. Li, An experimental investigation of pool boiling heat transfer on smooth/rib surfaces under an electric field, Int. J. Heat Mass Transf. 85 (2015) 595–608. https://doi.org/10.1016/j.ijheatmasstransfer.2015.01.083.

[151] A. Sur, Y. Lu, C. Pascente, P. Ruchhoeft, D. Liu, Pool boiling heat transfer enhancement with electrowetting, Int. J. Heat Mass Transf. 120 (2018) 202–217. https://doi.org/10.1016/j.ijheatmasstransfer.2017.12.029.

[152] H. Huang, Y. Tian, T. Wei, J. Qian, X. He, X. Cheng, AC electrowetting-on-dielectric induced vapor-liquid interface oscillation for flow boiling heat transfer enhancement in microchannels, Int. J. Therm. Sci. 210 (2025) 109638. https://doi.org/10.1016/j.ijthermalsci.2024.109638.

[153] H. Xu, J. Wang, Z. Wang, H. Wang, K. Yu, W. Zhang, L. Zuo, H.-B. Kim, Review of electrospray cooling and charged droplets heat transfer, Phys. Fluids 37 (2025) 111303. https://doi.org/10.1063/5.0299519.

[154] P.D. Marco, W. Grassi, Saturated Pool Boiling Enhancement by Means of an Electric Field, J. Enhanc. Heat Transf. 1 (1994). https://doi.org/10.1615/JEnhHeatTransf.v1.i1.90.

[155] S. Wang, A. Yazdekhasti, A. Alizadeh, A. Basem, D.J. Jasim, A.H. Al-Rubaye, S. Salahshour, D. Toghraie, Calculating minimum droplet diameter in dripping, spindle, and cone-jet modes based on experimental data in the electrospray process, Exp. Therm. Fluid Sci. 154 (2024) 111154. https://doi.org/10.1016/j.expthermflusci.2024.111154.

[156] J.A. Estrada-Díaz, I.B. Aguilar-Meza, D. Olvera-Trejo, A. Elías-Zúñiga, O. Martínez-Romero, Dimensional analysis for jet diameter prediction in electrospray: Integrating electric field and process parameters, J. Aerosol Sci. 185 (2025) 106540. https://doi.org/10.1016/j.jaerosci.2025.106540.

[157] Y. Kim, S. Jung, S. Kim, S.T. Choi, M. Kim, H. Lee, Heat transfer performance of water-based electrospray cooling, Int. Commun. Heat Mass Transf. 118 (2020) 104861. https://doi.org/10.1016/j.icheatmasstransfer.2020.104861.

[158] H.-C. Wang, A.V. Mamishev, Heat transfer correlation models for electrospray evaporative cooling chambers of different geometry types, Appl. Therm. Eng. 40 (2012) 91–101. https://doi.org/10.1016/j.applthermaleng.2012.01.061.

[159] S. Wang, A. Yazdekhasti, A. Alizadeh, A. Basem, D.J. Jasim, A.H. Al-Rubaye, S. Salahshour, D. Toghraie, Calculating minimum droplet diameter in dripping, spindle, and cone-jet modes based on experimental data in the electrospray process, Exp. Therm. Fluid Sci. 154 (2024) 111154. https://doi.org/10.1016/j.expthermflusci.2024.111154.

[160] M. Raissi, P. Perdikaris, G.E. Karniadakis, Physics-informed neural networks: A deep learning framework for solving forward and inverse problems involving nonlinear partial differential equations, J. Comput. Phys. 378 (2019) 686–707. https://doi.org/10.1016/j.jcp.2018.10.045.

[161] M. Raissi, A. Yazdani, G.E. Karniadakis, Hidden fluid mechanics: Learning velocity and pressure fields from flow visualizations, Science 367 (2020) 1026–1030. https://doi.org/10.1126/science.aaw4741.

[162] S. Cai, Z. Mao, Z. Wang, M. Yin, G.E. Karniadakis, Physics-informed neural networks (PINNs) for fluid mechanics: a review, Acta Mech. Sin. 37 (2021) 1727–1738. https://doi.org/10.1007/s10409-021-01148-1.

[163] A. Kashefi, T. Mukerji, Physics-informed PointNet: A deep learning solver for steady-state incompressible flows and thermal fields on multiple sets of irregular geometries, J. Comput. Phys. 468 (2022) 111510. https://doi.org/10.1016/j.jcp.2022.111510.

[164] X. Zhao, K. Shirvan, R.K. Salko, F. Guo, On the prediction of critical heat flux using a physics-informed machine learning-aided framework, Appl. Therm. Eng. 164 (2020) 114540. https://doi.org/10.1016/j.applthermaleng.2019.114540.

[165] A. Hazra, P. Sarkar, S. Sarkar, Physics-Informed Neural Networks for Estimating Convective Heat Transfer in Jet Impingement Cooling: A Comparison with Conjugate Heat Transfer Simulations, arXiv.Org (2025). https://arxiv.org/abs/2507.09356v1 (accessed June 24, 2026).

[166] H. Ding, X. Song, X. Chai, C. Wen, Y. Yang, Morphology and heat transfer of a train of microdroplets impinging on the heated surface for spray cooling, Int. Commun. Heat Mass Transf. 158 (2024) 107914. https://doi.org/10.1016/j.icheatmasstransfer.2024.107914.

[167] A. Han, R. Chiodi, O. Desjardins, Capturing thin structures in VOF simulations with two-plane reconstruction, J. Comput. Phys. 519 (2024) 113453. https://doi.org/10.1016/j.jcp.2024.113453.

[168] A. Han, O. Desjardins, Subgrid scale modeling of droplet bag breakup in VOF simulations, Int. J. Multiph. Flow 180 (2024) 104958. https://doi.org/10.1016/j.ijmultiphaseflow.2024.104958.

[169] A. Zeraatkardevin, S. Jowkar, M.R. Morad, X. Shen, A three dimensional simulation of spray cooling and its evaporating liquid film generated on patterned surfaces, Int. J. Multiph. Flow 155 (2022) 104174. https://doi.org/10.1016/j.ijmultiphaseflow.2022.104174.

[170] J.M. López-Herrera, S. Popinet, M.A. Herrada, A charge-conservative approach for simulating electrohydrodynamic two-phase flows using volume-of-fluid, J. Comput. Phys. 230 (2011) 1939–1955. https://doi.org/10.1016/j.jcp.2010.11.042.

[171] M. Rahmanpour, R. Ebrahimi, A. Pourrajabian, Numerical simulation of two-phase electrohydrodynamic of stable Taylor cone–jet using a volume-of-fluid approach, J. Braz. Soc. Mech. Sci. Eng. 39 (2017) 4443–4453. https://doi.org/10.1007/s40430-017-0832-7.

[172] H. Huh, R.E. Wirz, Simulation of electrospray emission processes for low to moderate conductivity liquids, Phys. Fluids 34 (2022). https://doi.org/10.1063/5.0120737.

[173] M. Gamero-Castaño, M. Magnani, Numerical simulation of electrospraying in the cone-jet mode, J. Fluid Mech. 859 (2019) 247–267. https://doi.org/10.1017/jfm.2018.832.

[174] Y. Guo, Y. Guan, B. He, Y. Sha, M. Wang, Z. Hu, Y. Lei, Numerical investigation into the transition of electrohydrodynamic spraying modes and behaviors, Phys. Fluids 36 (2024) 102005. https://doi.org/10.1063/5.0226478.

[175] S. Cândido, J.C. Páscoa, Dynamics of three-dimensional electrohydrodynamic instabilities on Taylor cone jets using a numerical approach, Phys. Fluids 35 (2023) 052110. https://doi.org/10.1063/5.0151109.

[176] A.K. Arumugham-Achari, J. Grifoll, J. Rosell-Llompart, Two-way coupled numerical simulation of electrospray with induced gas flow, J. Aerosol Sci. 65 (2013) 121–133. https://doi.org/10.1016/j.jaerosci.2013.07.005.

[177] A.K. Arumugham-Achari, J. Grifoll, J. Rosell-Llompart, A Comprehensive Framework for the Numerical Simulation of Evaporating Electrosprays, Aerosol Sci. Technol. 49 (2015) 436–448. https://doi.org/10.1080/02786826.2015.1039639.

[178] A. Brentjes, A.K. Pozarlik, G. Brem, Numerical simulation of evaporating charged sprays in spray chilling, J. Electrost. 107 (2020) 103471. https://doi.org/10.1016/j.elstat.2020.103471.

[179] J. Jiang, Z. Qian, X. Wang, H. Chen, G. Kang, Y. Liu, G. Zheng, W. Li, Numerical Simulation of Motion and Distribution Characteristics for Electrospray Droplets, Micromachines 14 (2023) 396. https://doi.org/10.3390/mi14020396.

[180] H. Wan, P.J. Liu, F. Qin, X.G. Wei, G.Q. He, W.Q. Li, Enhancing electrospray cooling via electrode ring: An experimental and numerical study, Int. J. Therm. Sci. 214 (2025) 109839. https://doi.org/10.1016/j.ijthermalsci.2025.109839.